Absolute Intercalibration of Spaceborne Microwave Radiometers

Katherine Wentz,[a] Thomas Meissner,[a] Frank Wentz,[a] and Andrew Manaster[a]

[a] *Remote Sensing Systems, Santa Rosa, California*

Corresponding author: Katherine Wentz, kwentz@remss.com.

ABSTRACT

Absolute calibration of spaceborne microwave radiometer observations consists of accurate determination of antenna cold space spillover, cross-polarization contamination, and nonlinearity coefficients of the receivers. We deem the GMI sensor to be the most accurate calibrated spaceborne microwave radiometer due to its unique calibration design features and its carefully planned orbit maneuvers. We demonstrate how to transfer the GMI calibration to other spaceborne radiometers, whose operations have sufficient time overlap with GMI. Specifically, we show results for WindSat and AMSR2. The sensor intercalibration is based on brightness temperature match-ups between GMI and the other instruments over both open ocean and rainforest scenes. In order to assess the calibration accuracy, we compare the intercalibrated brightness temperatures with radiative transfer model calculations. In addition, we provide in-situ validation results for wind speed and water vapor retrievals from the intercalibrated sensors. The intercalibration methodology allows for the creation of a multi-decadal climate data record from passive microwave satellite observations.

SIGNIFICANCE STATEMENT

Creating a long-term climate data record of satellite observations of ocean winds, water vapor, and other variables requires careful and accurate calibration of the various sensors that are used. In particular, it is important to achieve the best possible consistency between the measurements from all the different instruments. This is a challenging task as the configuration and accuracy of these instruments can differ widely. The purpose of our paper is to demonstrate and validate the basic methodology for performing this intercalibration. The backbone of our method are data observed by a well-calibrated sensor that measures the passive microwave emission from the Earth's surface and atmosphere. We show how to transfer its calibration standard to other sensors.

1. Introduction

Since 1987, spaceborne microwave imaging radiometers have been providing the scientific community with measurements of multiple environmental parameters over ocean, land, and ice surfaces. These include ocean surface wind vectors, sea-surface temperature (SST), columnar water vapor, columnar cloud liquid water, surface rain rate, soil moisture, and sea-ice thickness. Spaceborne passive microwave sensors that have operated or continue to operate include SSM/I (Hollinger et al. 1990), TMI (Kummerow et al. 2000), AMSR-E (Kawanishi et al. 2003), WindSat (Gaiser et al. 2004), SSMIS (Kunkee et al. 2008), AMSR2

(Oki et al. 2010), and GMI (Draper et al. 2015a). Creating a multi-decadal climate data record from these observations requires an accurate intercalibration of the brightness temperature (TB) observations that are the input to geophysical retrievals, and which originate from multiple operating sensors (Sapiano et al. 2013; Wentz 2015). The term *absolutely calibrated* refers to the value of the average TB over a large range of Earth scenes whose calibration is essentially independent of a radiative transfer model (RTM). The absolute calibration accuracy of any microwave radiometer is predominantly driven by the three factors given below (Meissner et al. 2012). Note, we assume that the errors arising from other factors are already largely corrected prior to performing intercalibration (Section 7).

1. The antenna spillover, which is the fraction of the antenna power gain that falls on cold sky, and thus measures the TB of the cosmic microwave background (CMB) radiation rather than the TB of the Earth scene.

2. Antenna cross-polarization contamination that mixes the TB of the vertical (V) and horizontal (H) polarizations and, if present, the polarimetric channels, which are the 3rd Stokes (S3) and the 4th Stokes (S4) parameters.

3. A non-linear behavior of the sensor receiver. This results from a deviation from the linear relationship between radiometer counts and antenna temperatures (TAs) that is otherwise assumed to hold within the dynamic range of radiometric temperatures between hot and cold calibration loads.

Ideally, the values of these calibration parameters can be determined during pre-launch campaigns and then used when the sensor is on-orbit. However, experience with most, if not all, past and presently operating microwave radiometers shows that it is difficult to do this to the necessary level of radiometric accuracy. This applies in particular to the pre-launch determination of the antenna spillover, which requires measuring the gain of the antenna backlobes. This signal is small, but it covers a large part of the antenna field of view. Therefore, for each sensor, the antenna spillover, the antenna cross-polarization contamination, and receiver non-linearity (NL) need to be assessed on-orbit or at least adjusted from their prelaunch values. This is the task of the post-launch absolute sensor calibration.

Among all spaceborne microwave radiometers that have operated since 1987, the GMI sensor (Draper et al. 2015a) is deemed to be the best calibrated one. This is mainly because of the superior design of the GMI calibration system (Draper et al. 2015b) and a carefully

executed series of on-orbit maneuvers that helped determine the calibration parameters (Wentz and Draper 2016). In particular:

1. A 4-point calibration system has been implemented for GMI (Draper et al. 2015b), which consists of an external hot and cold calibration load and an additional internal calibration using noise diode injection. The redundancy that is built into this system allows an on-orbit check of the values for the receiver non-linearities. It also allows a check to determine if the external hot calibration load is susceptible to solar intrusion, which can result in thermal gradients and thus inaccurate readings of the hot-load temperature.
2. After launch, a series of calibration maneuvers were performed on GMI (Wentz and Draper 2016). They included: (a) a deep space maneuver, during which both the main and the cold sky reflector were viewing cold space, for finding along-scan biases due to the external calibration sources, (b) a backlobe maneuver, during which the backlobes of the main reflector were viewing the Earth, for determining the TB contribution from cold space spillover, and (c) a nadir maneuver, during which the main reflector was viewing the Earth at an Earth incidence angle (EIA) of 0°, for disentangling biases in the V- and H-pol TB values from cross-polarization effects.
3. No significant calibration anomalies or drifts have been observed with GMI, such as solar intrusion into the hot calibration load (Twarog et al. 2006; Bell et al. 2008; Meissner et al. 2012; Wentz 2013), an emissive reflector antenna (Wentz et al. 2001; Bell et al. 2008; Wentz 2015), or temporal drifts in the calibration system (Wentz 2021). These issues have affected all other passive microwave sensors in some way.

An analysis of GMI observations that were taken during the calibration maneuvers as well as during normal operations showed that it was possible to absolutely calibrate GMI with a radiometric accuracy of about 0.2 – 0.3 K. This is significantly better than what has been achieved with any other passive satellite sensor using different calibration techniques, whose accuracies are typically in the order of one to a few Kelvin depending on the instrument and channel (Colton and Poe 1999; Kroodsma et al. 2012; Biswas et al. 2013).

The goal of our study is to demonstrate how the highly accurate absolute calibration of GMI can be transferred to other passive microwave sensors that have sufficient temporal overlap with GMI. We use the WindSat and AMSR2 sensors as specific examples. The core of the absolute intercalibration methodology are match-ups between TB observations that were taken by GMI and the other sensors over the open ocean and the Amazon rainforest.

Because the GMI orbit is not sun-synchronous and thus its ascending node time is constantly shifting, it is easy to create a sufficiently populated TB match-up dataset with the sun-synchronous AMSR2 and WindSat sensors. In this manuscript, we validate the radiometric intercalibration accuracy by comparing the calibrated TB data with calculations made by an RTM. In addition, we validate GMI, WindSat and AMSR2 wind speed and water vapor retrievals using calibrated TB with in-situ buoy and GPS measurements.

2. Methodology for absolute sensor intercalibration

a. Basic relations and parameters for sensor calibration

The task of calibrating a passive microwave sensor consists of the transformation of counts or voltages that are measured by the receiver into top of the atmosphere (TOA) TB. The procedure involves two major steps: (1) transforming radiometer counts into TA, and (2) transforming TA into TB.

1) RADIOMETER COUNTS TO TA

The basic relation between radiometer counts C_E that are received over a typical Earth scene E and their associated antenna temperature $T_{A,E}$ for a specific channel is given by:

$$T_{A,E} = x_E \cdot T_H + (1 - x_E) \cdot T_C - \Delta T_{NL} \qquad x_E = \frac{C_E - C_C}{C_H - C_C}, \tag{1}$$

where C_H are the counts taken over the hot calibration reference load, whose radiometric temperature is T_H and C_C are the counts taken over the cold reference load, whose radiometric temperature is T_C. For externally calibrated radiometers, T_C is the Planck effective brightness temperature of the cold sky, which is determined by the radiometric temperature of the CMB and includes a small deviation from the Rayleigh-Jeans law (Meissner et al. 2012). For each scan, the values of C_H, T_H, and C_C are measured and updated. If the responses of the receivers were perfect, the $T_{A,E}$ would be completely determined by the counts and temperature of the hot and cold calibration references and thus the first two terms on the r.h.s. of Equation (1). However, in reality, the receivers of all known spaceborne radiometers exhibit some small non-linear response, which needs to be taken into account when taking measurements over a wide dynamical range of Earth scenes ranging from the radiometrically cold ocean to radiometrically hot scenes over ice and land. The receiver NL response is denoted by term ΔT_{NL} in Equation (1). Typically, ΔT_{NL} is parametrized by a polynomial of the ratio x_E, which is tied to

zero at the cold and the hot ends. In most instances, a quadratic polynomial turns out to be sufficient and we use the parametrization:

$$\Delta T_{NL} = 4 \cdot a_{NL} \cdot x_E \cdot (1 - x_E), \tag{2}$$

which assumes its largest absolute value of $\Delta T_{NL} = a_{NL}$ at $x_E = ½$. The sign of the NL coefficient a_{NL} can be positive or negative. In the case of the AMSR2 sensor, it turns out that a quadratic parametrization is not adequate, and we need to use a higher order polynomial:

$$\Delta T_{NL} = \sum_{i=1}^{5} a_{NL,i} \cdot (x_E)^i \qquad \sum_{i=1}^{5} a_{NL,i} = 0. \tag{3}$$

In the computation of ΔT_{NL} in Equation (3), the count ratio x_E defined in Equation (1) can be accurately approximated by the temperature ratio $(T_{A,E} - T_C)/(T_H - T_C)$, because ΔT_{NL} is small compared to $T_{A,E}$ and T_H. This ensures that $\Delta T_{NL}(T_C) \approx \Delta T_{NL}(T_H) \approx 0$ in Equations (2) and (3), as desired.

2) TA TO TB

The relationship between TA and TOA TB is commonly referred to as antenna pattern correction (APC) and is most intuitively written as a forward model, i.e., going from a physical scene (TB) to an antenna measurement (TA). It consists of two parts: (1) The cross-polarization mixing and (2) the antenna spillover.

The cross-polarization mixing can be parameterized as a linearization of the antenna gain pattern integral (Piepmeier et al. 2008; Meissner et al. 2012). In the modified Stokes basis (V, H) it reads:

$$\begin{pmatrix} T_{AV}' \\ T_{AH}' \end{pmatrix} = \mathbf{C} \cdot \mathbf{R}(\omega) \cdot \begin{pmatrix} T_{BV} \\ T_{BH} \end{pmatrix} \qquad \mathbf{C} = \begin{pmatrix} C_{VV} & 1 - C_{VV} \\ 1 - C_{HH} & C_{HH} \end{pmatrix}. \tag{4}$$

The elements of the matrix **C** describe the antenna cross-polarization contamination. We have omitted S3 and S4 because GMI and AMSR2 do not measure S3 and S4 radiances, and we are only considering the S1 and S2 channels for WindSat in this manuscript because the values of S3 and S4 are small compared to V/H-pol. The matrix $\mathbf{R}(\omega)$ denotes a rotation matrix between the V/H polarization basis of the antenna and the Earth scene. The rotation angle $\omega = \omega_{geom} + \omega_F$ is the sum of a geometrical alignment difference of the V and H polarization vectors in the antenna and Earth frames (ω_{geom}) and the Faraday rotation of the polarized electromagnetic radiation when travelling through the Earth's ionosphere (ω_F) (Meissner

and Wentz 2006a). The rotation matrix $\mathbf{R}(\omega)$ effectively mixes the S2 (V – H) and the S3 components of the TB vector. For our purposes, we will set the rotation angle ω to zero and thus, **R** to the unity matrix in Equation (4). This is justified because: (1) for the Earth scenes that we will consider, the numerical value of S3 is small compared to S2, and (2) the values of the polarization angles ω_{geom} and the Faraday rotation angles ω_F are small for the GMI, AMSR2, and WindSat frequency bands that we will use in our investigation.

The second part of the TB to TA transformation describes the power loss that is caused by parts of the antenna backlobes falling on cold sky, whose brightness temperature is denoted as T_C. The cold sky fraction of the antenna gain pattern is called the antenna spillover η, which means:

$$T_A = (1-\eta)\cdot T_A' + \eta \cdot T_C. \quad (5)$$

The value of η depends on frequency and also on polarization, though for most real antenna patterns one observes $\eta_V \approx \eta_H$.

The transformation going from the measured TA to the TOA TB is obtained by successively inverting the two linear transformations in Equations (5) and (4).

b. On-orbit intercalibration scheme and algorithm

The calibration of a passive microwave sensor consists of the determination of the parameters η, $\mathbf{C}_{ij}$ and $a_{NL,i}$. In order to achieve absolute calibration of microwave sensors, the objective is to transfer the absolute calibration of the target sensor, GMI, to the new sensors by calibrating these three parameters. In this paper, we will show the results of the intercalibration methodology for the WindSat and AMSR2 sensors. Fig. 1 shows the basic steps that are involved in the intercalibration parameter training (solid lines; orange boxes) and validation (dotted lines).

The absolute calibration parameters η, $\mathbf{C}_{ij}$ and $a_{NL,i}$ of the sensor S, either AMSR2 or WindSat, are found by minimizing the sum of squares χ^2 between the adjusted GMI TB with the TB measurements of S, which are determined by radiometer count measurements and the set of transformations from Section 2a (Equation (6)). Note that the center frequencies and Earth-incidence angles of the GMI, WindSat, and AMSR2 channels are slightly different, which needs to be taken into account when matching the TB measurements. Thus, it is necessary to adjust the GMI TB measurements to the configuration of the other sensors using an RTM ($T_{B,adj}$). Details will be explained in Section 4e.

$$\chi^2 = \left[T_{B,adj}\left[GMI\right] - T_{B,meas}\left[S\right](\eta, \mathbf{C}, a_{NL}) \right]^2 . \quad (6)$$

As the dependence of the TB on the absolute calibration parameters is linear, the minimization of χ^2 in Equation (6) amounts to determining these parameters through linear regressions in each frequency band. A computationally effective method is to first consider only rainforest scenes, whose TB is on the order of 280–290 K, which is close to the radiometric temperature T_H of the hot calibration load and is therefore unaffected by non-linearity. Furthermore, the rainforest TB is almost independent of polarization and thus not affected by cross-polarization contamination. This allows for a straightforward determination of the spillover values η. Once the spillover has been fixed, we need to perform the regressions for $\mathbf{C}_{ij}$ and $a_{NL,i}$ for TB match-ups over open ocean scenes only. The results of the regressions have no significant impact on the TB values near or at the hot end.

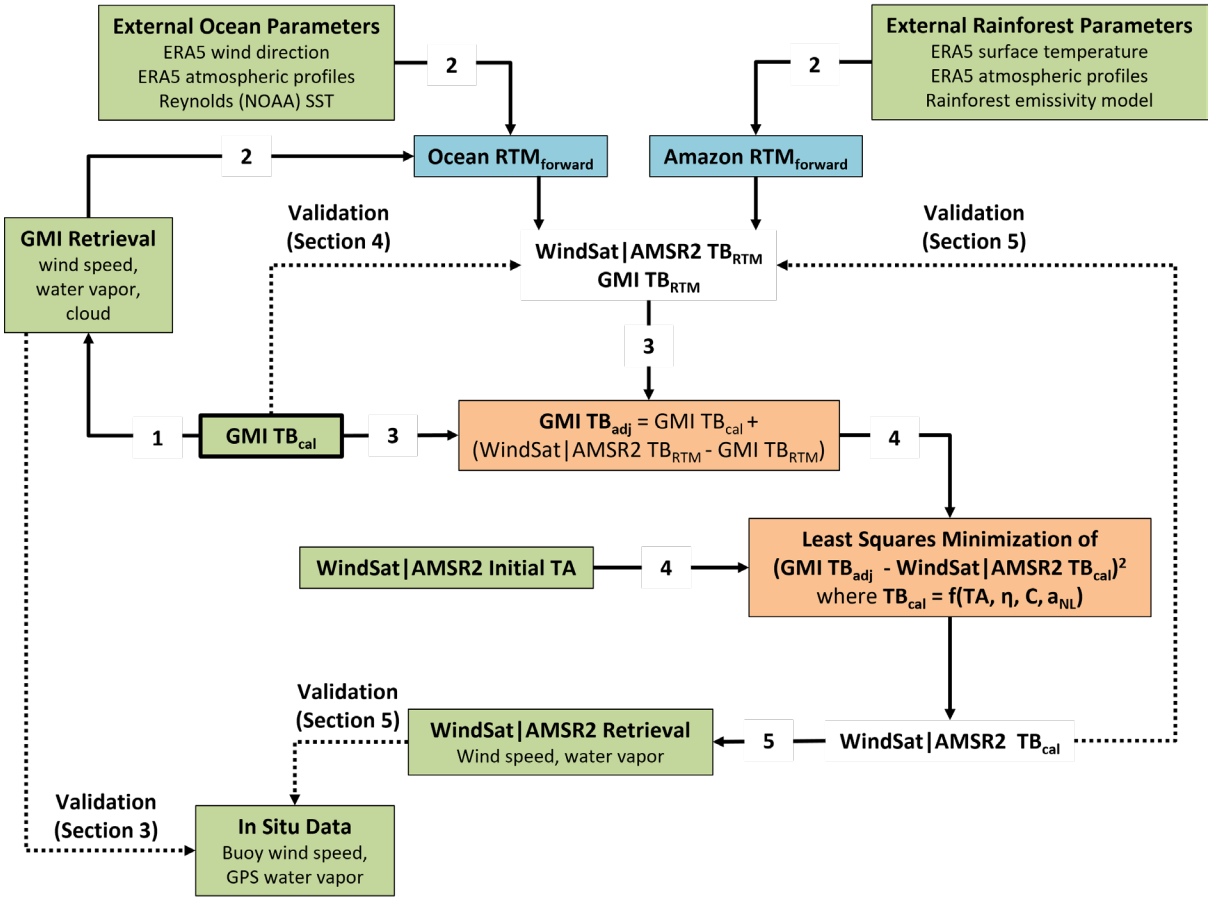

Fig. 1. Schematic algorithm flow for intercalibrating TB from a passive microwave sensor (WindSat | AMSR2) to GMI TB. The numbers show the order of steps, starting from the bolded **GMI TB$_{cal}$** box in green. The green boxes show the datasets used in the analysis (Section 3), the blue boxes show the RTM contributions (Section 4), and the orange boxes show key aspects of the intercalibration methodology (Section 2). In Step (1), absolutely calibrated

GMI TB are used to retrieve GMI geophysical variables. Step (2) calculates RTM TB for GMI, WindSat, and AMSR2 over the ocean and Amazon rainforest. Step (3) finds the adjusted GMI TB with the same EIA and frequency bands as WindSat | AMSR2. Step (4) inputs the adjusted GMI TB and the WindSat | AMSR2 TA into the linear least squares regression, which then solves for the calibration parameters that minimize the difference between WindSat | AMSR2 TB and GMI TB. Step (5) uses the WindSat | AMSR2 TB to retrieve geophysical variables. The dotted lines indicate the points at which the intercalibration is validated, along with the sections where that validation is presented.

3. Satellite measurements and ancillary data

This section describes the datasets used in the intercalibration methodology (green boxes in Fig. 1). These datasets include those that are used to find the calibration parameters and those that are used to validate the TB results and retrieval results using the trained calibration parameters.

a. Data for intercalibration training and validation at the TB level

The following datasets are used to intercalibrate WindSat and AMSR2 TB with GMI TB over the open ocean and rainforest. The time window for a valid match-up collocation is 1 hour. For the rainforest target, we have chosen observations that fall within a box bounded by the coordinates (1S, 3N) and (52W, 59W), which is located over the Amazon rainforest (Brown and Ruf 2005; Meissner and Wentz 2010; Wentz 2015). This area is characterized by hot TB values, which show relatively small inter-annual variations, and a thick rainforest canopy, which make the emitted TB almost independent of EIA. Notably, the rainforest exhibits large swings in TB (up to 10 K) depending on the time of day. The 1-hour time window for matchups between GMI and WindSat/AMSR2 data reduces errors associated with the diurnal differences in temperature between the two datasets. In addition, we use ancillary datasets to model the diurnal variation in the Amazon rainforest RTM (Sections 4c and 4d). The time ranges of our analysis comprise the years 2014 – 2016 for intercalibration and 2017 – 2019 for TB validation.

1) GMI BRIGHTNESS TEMPERATURES

The target of the sensor intercalibration are TOA TB measured from GMI (GPM Science Team 2022; Table 1). GMI is dual-polarized (V/H-pol) at all bands at or below 89 GHz except at the 23 GHz band, which is only V-pol. GMI has higher frequency channels above 89 GHz, which we will not consider in this study. The GMI scan contains forward looking Earth

observations only. The calibration of the GMI TB has been derived in detail by Wentz and Draper (2016).

Band	10	18	23	36	89
Pol	V H	V H	V	V H	V H
f_{center} (GHz)	10.65	18.69	23.81	36.64	89.0
EIA_{ave} (°)	52.75				

Table 1. GMI channel configuration passband center frequencies f_{center} and average Earth incidence angles EIA_{ave}. The values for f_{center} were provided by the Calibration Data Book for GMI (D. Draper, 2015, Ball Aerospace and Technologies Corp. Tech. Rep. 2344649, Version G, unpublished). The polarizations are V = vertical, H = horizontal.

The calibrated GMI TB for each channel are first resampled along-scan to the footprint with the coarsest resolution (the 10 GHz band) using the Backus-Gilbert Optimum Interpolation (OI) technique (Poe 1990; Ashcroft and Wentz 2000). Exceptions are the 89 GHz channels, which are resampled to the 36 GHz resolution. This OI resampling is not essential for performing the absolute calibration, but it reduces the radiometer noise in the forthcoming error analysis. The resampled TB are then straight averaged onto a regular 0.25° latitudinal and longitudinal Earth grid and arranged into daily maps separately for ascending and descending swaths. If observations from more than one orbit fall into the same grid cell, we only take the observations at the latest time.

2) WindSat antenna temperatures

WindSat takes fully polarimetric measurements at the 10, 18, and 37 GHz bands (Table 2). Each of these fully polarimetric bands has 3 feeds measuring V/H, plus(P)/minus(M) 45-degrees, and left(L)/right(R) circular polarizations. The 6 and 23 GHz bands only have dual polarization (V/H-pol). We will not consider the polarimetric WindSat channels in this study. Note that the passband center frequencies for V- and H-pol at 18 GHz differ by about 50 MHz. The WindSat scan contains both fore- and aft-looking Earth observations.

Band	6	10	18		23	37
Pol	V H	V H	V	H	V H	V H
f_{center} (GHz)	6.80	10.71	18.68	18.73	23.80	37.02

EIA_{ave} (°)	53.711	50.080	55.573	53.206	53.202

Table 2. WindSat channel configuration passband center frequencies f_{center} and average Earth incidence angles EIA_{ave}. The values for f_{center} are approximated from the passband response functions that were provided by Bettenhausen and Gaiser (2014) and are based on prelaunch measurements. The polarizations are V = vertical, H = horizontal.

Intercalibration begins with WindSat L1A radiometer data, which contain Earth counts, calibration counts, hot load thermistor readings, spacecraft ephemeris, and sensor pointing information. The L1A data were provided to us by the U.S. Naval Research Laboratory (NRL) upon special request. Applying the standard counts to the TA transformation from Section 2a (Equation (1)), these Earth counts are turned into TA. However, we do not apply the NL correction ΔT_{NL} yet as determining this value is part of the absolute calibration task. In order to achieve TB noise figures that are comparable to the other sensors, the TA of the various channels are OI resampled onto a fixed regular 0.125° Earth grid at the 10 GHz spatial resolution prior to intercalibration (Meissner et al. 2022). The 6 GHz TAs are left at their native resolution. To allow an easy match-up with the GMI TB, the resampled WindSat TAs are then also straight averaged into regular 0.25° latitudinal and longitudinal Earth grid cells and arranged into daily maps. We produce separate maps for ascending and descending swaths and for fore and aft looks.

3) AMSR2 ANTENNA TEMPERATURES

AMSR2 is dual-polarized (V/H-pol) at all bands and the scan contains forward looking Earth observations only (Table 3). At 89 GHz, observations are taken by two feedhorns, labelled horn A and horn B, whose off-nadir angles are slightly offset from each other to optimize ground coverage. As with WindSat, we start with L1A radiometer data (JAXA 2012a). The Earth counts are then transformed into TA assuming a linear response Equation (1) without applying the NL term ΔT_{NL}. We perform an OI resampling along-scan similar to how it was done for the GMI TB. Finally, the AMSR2 TAs are straight averaged onto a regular 0.25° Earth grid, separated by ascending and descending passes (Meissner et al. 2023).

Band	6	7	10	18		23		36	89A	89B
Pol	V H	V H	V H	V	H	V	H	V H	V H	V H
f_{center} (GHz) *nominal*	6.925	7.3	10.65	18.7		23.8		36.5	89.0	

f_{center} (GHz) *real*	6.925	7.3	10.65	18.7	18.6	23.73	23.8	36.5	89.0	
EIA_{ave} (°)	55.0									54.49

Table 3. AMSR2 channel configuration passband center frequencies f_{center} and average Earth incidence angles EIA_{ave}. The nominal center frequency differs from the real center frequency for 18 and 23 GHz as described in Section 5b. The polarizations are V = vertical, H = horizontal.

4) Ancillary data for the RTM computation

Several ancillary datasets are required for the RTM, both for the adjustment of TB in the intercalibration methodology and for validation. The ancillary data are linearly interpolated to the time and location of the satellite TB grid cell, except the ERA5 fields for which the field at the hour closest to the satellite observation is used. The following ancillary datasets are also required for quality control. Moreover, in order to minimize spurious biases in the RTM calculation for open ocean scenes, we filter out rain, land, sea ice, sun glitter, and radio frequency interference (RFI) from any known sources.

(i) GMI ocean parameters

The RTM requires GMI Version 8.2 Level 3 retrievals of ocean surface wind speed W, columnar water vapor V, columnar cloud liquid water L, and surface rain rate R (Wentz et al. 2015). The retrieval algorithm follows the method outlined by Wentz and Meissner (2007). The GMI ocean retrievals have the same time stamp as the GMI TB and we have gridded them in the same way as the GMI TB.

(ii) Surface temperatures

For ocean scenes, we use the daily NOAA Optimum Interpolated (OI) SST (Reynolds et al. 2002; NOAA 2020; Huang et al. 2021). For the rainforest scenes, we use the hourly skin temperature variable from ERA5 (ECMWF 2019).

(iii) Atmospheric profiles

The RTM atmospheric parameters τ (atmospheric transmittance), T_{BU} (upwelling atmospheric brightness temperature), and T_{BD} (downwelling atmospheric brightness temperature) are computed as weighted vertical integrals over the absorption coefficients $\alpha(h)$ for atmospheric absorption from water vapor, dry air (oxygen and nitrogen), and liquid cloud droplets

(Wentz and Meissner 2000), where h denotes the vertical height above the surface. The absorption coefficients $\alpha(h)$ are determined from the vertical atmospheric profiles for air temperature $T(h)$, air pressure $p(h)$, water vapor density $\rho_V(h)$, and cloud liquid water density $\rho_L(h)$. Our sources for these data come from the ERA5 vertical atmospheric profiles, which are provided hourly on a regular global 0.25° grid at 32 atmospheric levels (ECMWF 2019). Over the open ocean, we have scaled the vertical ERA5 profiles for $\rho_V(h)$ and $\rho_L(h)$ so that the total vertical integrals match the total columnar GMI values for V and L, respectively. This scaling is performed because the uncertainties of the ERA5 columnar values are expected to be larger than the uncertainties of the GMI values. No GMI retrievals for V and L are available for rainforest scenes, and we use the original ERA5 profiles for $\rho_V(h)$ and $\rho_L(h)$ in these instances.

(iv) Rain rates

Our analysis is designed for rain-free observations only. IMERG rain rates (Huffman et al. 2019), which are provided globally on a regular 0.1° grid every 30 minutes, are used for flagging and screening for precipitation.

(v) Ocean surface wind direction

Values for the ocean surface wind direction are taken from ERA5 10-meter neutral stability wind fields (ECMWF 2019).

(vi) Ocean surface salinity

For ocean surface salinity, we use the top layer value from the operational ocean analysis that is run by the U.S. Navy (HYCOM 2014).

b. Data for intercalibration validation at the retrieval level

The final step in the absolute calibration of each sensor consists of validating the ocean parameters that are retrieved from the intercalibrated TB versus independent in-situ ground truth measurements. This section gives a brief overview of the validation data sources and methods. The time range of our retrieval validation comprises the years 2017–2019.

1) GMI, WINDSAT, AND AMSR2 OCEAN RETRIEVALS

We use Remote Sensing Systems' Version 8 WindSat and Version 8.2 AMSR2 Level 3 retrievals of ocean surface low frequency wind speed W and columnar water vapor V to validate the absolute calibration of TB (Wentz et al. 2013; Wentz et al. 2014). The retrieval

algorithm follows the method outlined by Meissner and Wentz (2006b) and Wentz and Meissner (2000; 2007). It is a physically based multi-stage regression algorithm, which aims to determine *W* and *V* by minimizing the sum of squares between TOA TB that are measured by the sensor and the ones computed by the RTM. The retrieved ocean parameters have been gridded onto a regular 0.25° Earth grid and are separated by ascending and descending passes. Sea ice-, rain-, and land-contaminated scenes are removed from the validation dataset. To validate GMI retrievals, we use the same dataset that is ingested by the RTM.

2) IN-SITU DATA

(i) Buoy wind measurements

The in-situ measurements of ocean surface wind speed are taken from buoy datasets containing data from over 200 moored buoys distributed over the global ocean. We collected collocations between satellite winds and buoy observations from three sources. The first source is the National Data Buoy Center (Portmann 2009; NDBC 2023) with data from the Tropical Atmospheric Ocean (TAO) buoy array (McPhaden et al. 1998) in the Pacific Ocean. The second source is the Pacific Marine Environmental Laboratory (PMEL 2023), which includes buoys from the Pilot Research Moored Array in the Tropical Atlantic (PIRATA) (Bourlès et a. 2008) and the Research Moored Array for African-Asian-Australian Monsoon Analysis (RAMA) in the Indian Ocean (McPhaden et al. 2009). The third source is the Canadian Marine Environmental Data Section (MEDS; Gower 2002; DFO 2023).

For a valid satellite/buoy wind collocation, we required that the satellite wind measurement fall within +/-30 minutes of an hourly-averaged buoy observation. We discarded observations if the average satellite/collocated buoy wind speed was > 15 m s^{-1}, as buoys can be negatively impacted by buoy tilting, high sea state, and wave-sheltering at higher wind speeds. All buoy measurements were converted to 10-meter neutral stability winds using a logarithmic profile in order to compare to the satellite winds. Details on the methodology of collocating and comparing buoy and satellite wind measurements are given in Mears et al. (2001); however, it should be noted that in our analysis we used a nearest neighbor approach to collocate buoy observations rather than the interpolation method.

(ii) GPS water vapor measurements

The GPS water vapor data were acquired from the Nevada Geodetic Laboratory (Blewitt et al. 2018; NGL 2023). Our validations are based on a subset of stations located on small

islands. This aims to minimize possible land contamination. For a valid satellite – GPS collocation, we required that the satellite vapor measurements fall within +/-30 minutes of an hourly-averaged GPS observation. Note that the values of the GPS columnar vapor measurements needed to be adjusted to account for the difference between the height of the GPS station and the Earth's surface in order to accurately reflect the total columnar water vapor measured by the satellites which they are being compared to. We follow the methodology outlined in Mears et al. (2015) to perform this correction.

3) In-Situ Validation of GMI Retrievals

With the aforementioned in-situ datasets, we are able to perform in-situ validation of the GMI wind speeds and columnar water vapor used in the RTM for adjusting GMI TB. The results are shown in Fig. 2. The high accuracy (0.92 m s^{-1} wind speed RMSE and 1.64 mm water vapor RMSE) and absence of significant biases (– 0.05 m s^{-1} wind speed bias and 0.61 mm water vapor bias) between satellite and ground truth measurements justifies using the GMI observations as input to the RTM computations.

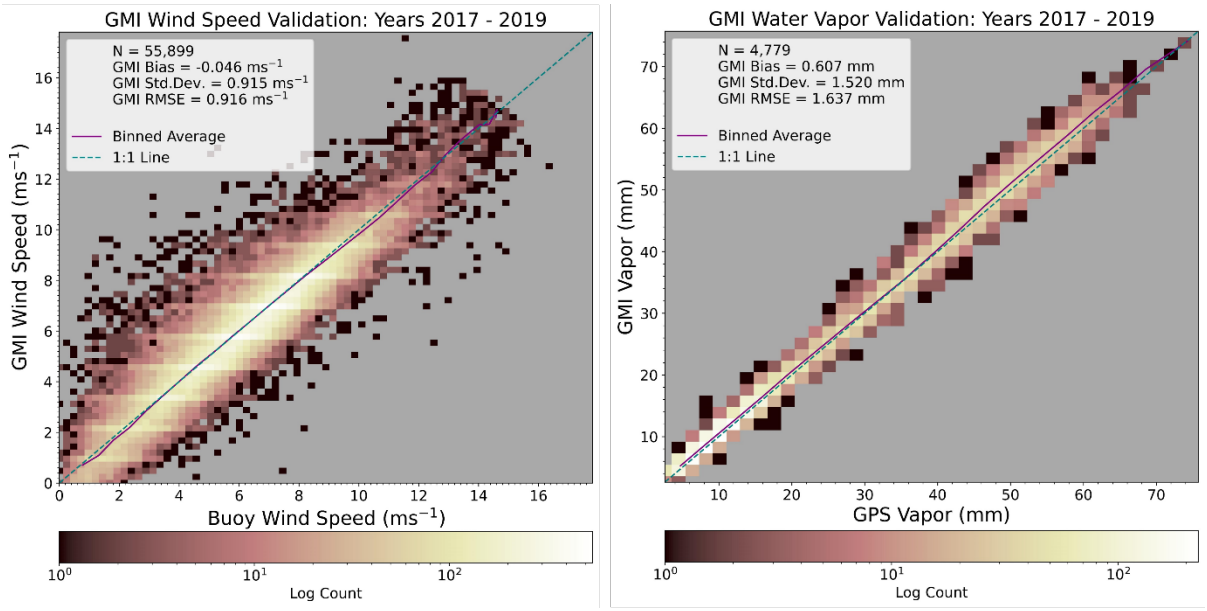

Fig. 2. Scatterplots of GMI versus buoy wind speeds (left) and GMI versus GPS columnar water vapor (right).

4. Radiative transfer models for open ocean and rainforest scenes

This section describes the ocean and Amazon rainforest RTMs used in the intercalibration methodology (blue boxes in Fig. 1). Both of these RTMs are primarily used for validating the intercalibration methodology and secondarily used to adjust the GMI TB to match EIAs and frequencies of WindSat/AMSR2.

a. Radiative transfer model for open ocean scenes

The RTM equation for the TOA TB of ocean scenes is given by (Wentz and Meissner 2000):

$$T_B = T_{BU} + \tau \cdot E \cdot T_S + \tau \cdot (1-E) \cdot \left[(1+\Omega) \cdot \left(T_{BD} - (1-\tau) \cdot T_C \right) + T_C \right]. \quad (7)$$

Here, T_S denotes SST and E denotes the microwave emissivity of the rough ocean surface. The Ω-term, also known as atmospheric path length correction, is a parameterization to correct for the contribution of the downwelling radiation that is scattered at the rough ocean surface from non-specular directions.

The ocean surface emissivity E is the sum of E_0, the emissivity of a flat ocean surface, and ΔE_W, the wind-induced emissivity of the rough ocean surface. Our study uses the dielectric sea-water model of Meissner and Wentz (2004; 2012) with the small update provided by Meissner et al. (2014) for the computation of E_0, and the wind-induced emissivity model of Meissner and Wentz (2012) for the computation of ΔE_W.

The atmospheric components of the RTM are determined by the absorption of microwave radiation by water vapor, dry air, and cloud water. As we consider only non-raining atmospheres, scattering by rain drops can be neglected and the Rayleigh approximation can be used for calculating the cloud water absorption (Wentz and Meissner 2000). The computation of the water vapor and dry air absorption coefficients is based on the microwave absorption model by Wentz and Meissner (2016). A few minor updates and adjustments have been made to this model, which are summarized in Appendix A.

The environmental parameters that serve as input to the ocean RTM calculation and their sources have been described in Section 3a. In the following, we compare GMI TB with the ocean RTM as an example of how we validate the WindSat and AMSR2 intercalibration in Section 5.

b. The 2V – H TB combination

When comparing measured TB with RTM calculations over the ocean at K-band (18–27 GHz) and higher frequencies, the atmospheric input can constitute a significant source of error. That applies particularly to the values for columnar cloud liquid water L and, to a lesser extent, the columnar water vapor V. For instance, at 37 GHz and an EIA of 55°, an error of 0.01 mm in L translates into an approximate TB error of 0.4 K for V-pol and 0.8 K for H-pol. That being said, the estimated uncertainty for cloud water retrievals from microwave satellite retrievals is at least 0.01 mm (Wentz 1997; Wentz and Meissner 2000). In order to minimize spurious errors in the TB calculation that are caused by uncertainties in the atmospheric input, we consider the channel combination $2 \cdot T_{B,V} - T_{B,H}$ in each frequency band rather than the TB of the single V-pol and H-pol channels. This combination is known to be less sensitive to atmospheric errors (Meissner and Wentz 2002). We multiply the combination by *1/sqrt(5)* when computing the standard deviation of the *2V – H* error in order to account for the proper normalization of the TB combination assuming random error.

Table 4 and Fig. 3 show the results for the absolutely calibrated minus RTM TB of the dual frequency GMI bands using the *2V – H* combination. Note that the undulating nature of the TB errors when binned by wind speed in Fig. 3 is likely a result of uncertainty in the RTM surface roughness model which models ocean surface emissivity as a function of a fifth-degree polynomial in wind speed. Overall, the absolute RTM biases are within 0.31 K. We aim to achieve similar levels of accuracy for the intercalibrated TB from WindSat and AMSR2.

Band	10	18	37	89
Bias	+0.09	+0.31	-0.02	+0.22
Std.Dev.	0.32	0.26	0.23	0.51

Table 4. Global statistics for GMI measured minus RTM TB over the open ocean using the combination *2V – H* for the bias and (*2V – H*)/sqrt(5) for the standard deviation of the error. All values are in Kelvin.

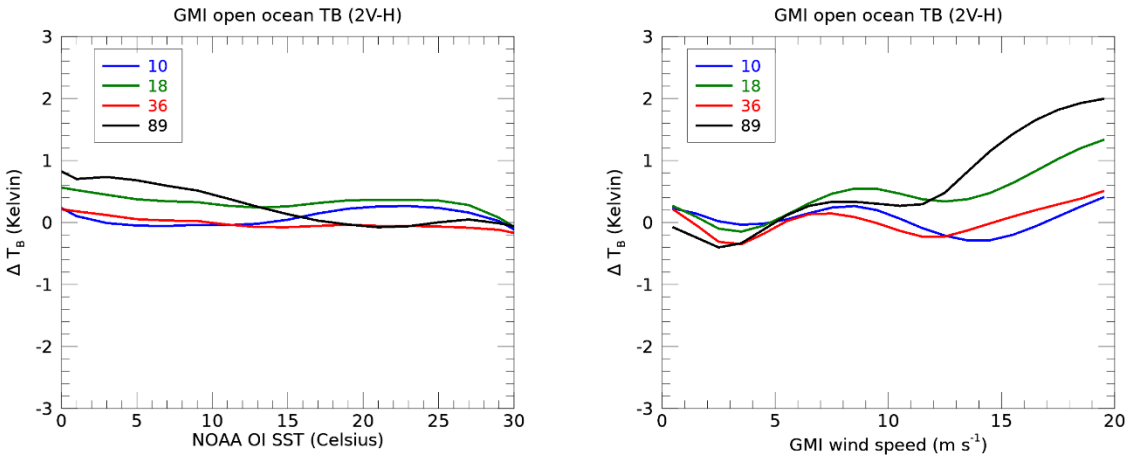

460

461 Fig. 3. Measured minus RTM TB *2V – H* over the open ocean for the dual polarized GMI
462 bands (10, 18, 36, 89 GHz) shown over a wide range of NOAA OI SSTs (left) and GMI wind
463 speeds (right).

464

465 *c. Radiative transfer model for rainforest scenes*

466 For the microwave frequency range of interest, we can model the radiation that is emitted
467 from the canopy of the Amazon rainforest scene as surface emission whose effective emissiv-
468 ity is given by $E = 1 - \omega$, where ω is the single scattering albedo of the rainforest canopy
469 (Meissner and Wentz 2010; Wentz 2015; Yang et al. 2016). The RTM for the TOA TB of the
470 rainforest scene (Njoku and Li 1999; Brown and Ruf 2005; Mo 2007) simplifies to:

471 $$T_B = T_{BU} + \tau \cdot E \cdot T_S + \tau \cdot (1 - E) \cdot [T_{BD} + \tau \cdot T_C]. \quad (8)$$

472 The inputs to the rainforest RTM are T_S and the atmospheric parameters T_{BU}, T_{BD}, and τ.
473 These variables are provided by ancillary fields of ERA5 (Section 3a). In order to solve for
474 emissivity, we have fit a simple model using these ERA5 inputs and GMI TB data which de-
475 scribes the dependence of $E(f)$ on the frequency f (in GHz):

476 $$E(f) = \sum_{i=0}^{4} B_i \cdot (f - 37)^i, \quad (9)$$

477 where $B_1 = 0$.

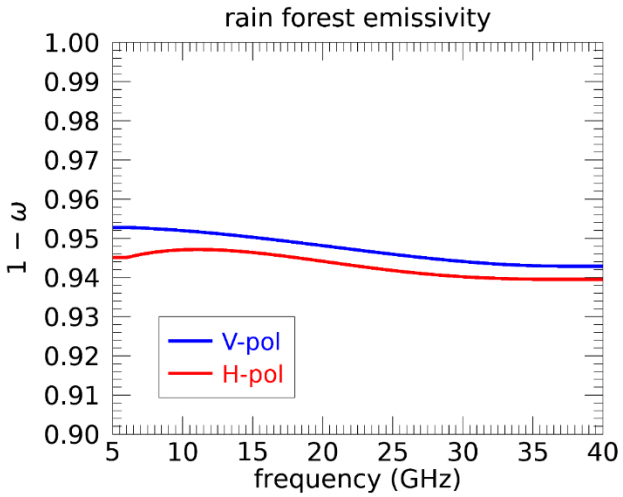

Fig. 4. Model for the effective emissivities $E = 1 - \omega$ of the rainforest scene as a function of frequency and based on GMI TB. Blue: V-pol. Red: H-pol. Above 37 GHz the values for $E(f)$ are kept constant. Note that the curves have been extrapolated below 10.7 GHz.

Fig. 4 shows the resulting curves for $E(f)$. The dependence of E on f over the whole frequency range is weak. The effective emissivity of the H-pol is slightly smaller than for the V-pol, which results in the H-pol TB being about 1 K lower than the V-pol TB. We use this simple model for the emissivity term in the Amazon rainforest RTM. In order to validate TB over the rainforest, we use the average $(V+H)/2$ TB as shown by the GMI example in the following. Note, we are neglecting the E dependence on EIA for the relevant angle range of 49° – 56°.

d. Diurnal variability of rainforest TB

The TB signal over the Amazon exhibits a diurnal variation of 5–10 K, depending on frequency (Mo 2007), which is caused by the diurnal variation of surface temperature, atmospheric temperature, moisture, and clouds. Over the daily cycle, it is instructive to assess how well the satellite TB observations are modelled by the RTM calculation (Equations (8) and (9)) using the ERA5 ancillary input. The shifting ascending node time of GMI makes this sensor the best candidate to study the diurnal TB signal over the rainforest scene.

Fig. 5 shows the excellent agreement between GMI observed and modeled 10 GHz TB variations over the rainforest as a function of local time. The values for the total statistics are listed in Table 5. All of the channel absolute biases are within 0.04 K except for 89 GHz which has a value of 0.71 K. This is in part due to cloud contamination that is not caught by the ERA5 dataset. Cloud coverage is common over the Amazon rainforest. The cloud

absorption for various frequencies is inversely related to wavelength, e.g., 89 GHz contains 2.5 times the amount of cloud absorption as compared to 37 GHz. Therefore, there is greater potential for cloud contamination in the 89 GHz channel TB.

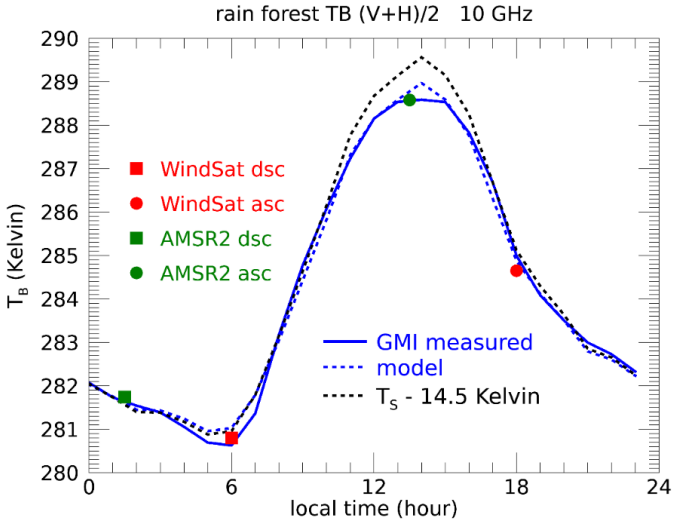

Fig. 5. Diurnal variation of the 10 GHz for *(V+H)/2* TB over the rainforest scene. The curves show the GMI observations (full blue), the results of the RTM (dashed blue) and the variation of the surface temperature (black dashed; decreased by 14.5 K in order to align with the measured and modeled TB). The symbols indicate the results for the ascending (circle) and descending (square) WindSat (red) and AMSR2 (green) TB.

Band	10	18	23	37	89
Bias	-0.01	-0.04	-0.04	-0.01	0.71
Std.Dev.	1.36	1.25	0.96	1.17	1.57

Table 5. Statistics for GMI measured minus RTM TB over the rainforest scene for *(V+H)/2*. In case of the single-polarized 23 GHz channel, the V-pol value is used. All values are in Kelvin.

e. TB adjustment for differences in channel configuration

When matching the TB measurements of GMI with the sensors that are going to be inter-calibrated to GMI, it is necessary to account for small differences in the channel configurations between GMI and these other sensors, which manifest themselves as slightly different values for center frequency and EIA. This is particularly important for matching the TB over open ocean scenes, where the frequency and EIA differences can result in TB differences of a

few Kelvin. We adjust the GMI TB to the configuration of the other sensor, labelled S, using the TB difference that is calculated from the ocean RTM:

$$T_{B,adj}\left(\mathrm{GMI}\right) = T_{B,meas}\left(\mathrm{GMI}\right) + \left[T_{B,RTM}\left(\mathrm{S}\right) - T_{B,RTM}\left(\mathrm{GMI}\right)\right]. \quad (10)$$

This adjustment method is frequently referred to as the double difference (DD) method (Kroodsma et al. 2012; Biswas et al. 2013).

We want to emphasize that the described method only uses the differences of the RTM calculations between channels within a very limited center frequency (100–500 MHz) and EIA range (49°–56°). The TB differences do not change significantly when a different RTM is used for computing them, as long as common emission and atmospheric absorption models are used. As the absolute GMI calibration does not use an RTM either, it follows that our proposed absolute sensor intercalibration method of using adjusted TB for GMI does not significantly depend on the choice of any specific RTM. Nonetheless, when comparing the absolutely calibrated TB with RTM-calculated TB, the result will of course depend on the RTM that is used in the comparison.

We note that for the WindSat and AMSR2 C-band channels (6 and 7 GHz) and the 23H channels, there are no matching channels for GMI and therefore no absolute intercalibration of their TB can be done. Rather, the calibration results presented in this manuscript were obtained by performing a calibration to the RTM. We have included the results for these channels for completeness.

5. Absolute calibration of WindSat and AMSR2

a. Calibration parameters

As laid out in Section 2b, the absolute calibration parameters for WindSat and AMSR2 are found by a linear regression, which amounts to performing the least squares minimization of the expression χ^2 in Equation (6). The resulting values for $1 - \eta$, $\mathbf{C}_{ij}$, and a_{NL} are listed in Table 6 for WindSat and Table 7 for AMSR2. The values for the AMSR2 coefficients $a_{NL,i}$ are listed in Table 13 in Appendix B.

Band	6	10	18	23	37
$1 - \eta_V$	0.97661	0.98571	0.98466	0.98460	0.98432
$1 - \eta_H$	0.97613	0.98468	0.98409	0.98396	0.98387

$\mathbf{C}_{VV}$	0.9935	0.9961	0.9939	0.9870	0.9953
a_{NL}	0.000	0.018	0.573	0.613	0.607

Table 6. Values for WindSat $1 - \eta$, WindSat V/H cross-polarization matrix elements $\mathbf{C}_{VV} = 1 - \mathbf{C}_{VH}$ and $\mathbf{C}_{VV} = \mathbf{C}_{HH}$, and WindSat non-linearity coefficients a_{NL} in Kelvin (Equation (2)). Note, the a_{NL} values for V- and H-pol are the same.

Band	6	7	10	18	23		36		89AB
Pol	V H	V H	V H	V H	V	H	V	H	V H
$1 - \eta$	0.975	0.972	0.978	0.981	0.980	0.979	0.977	0.976	0.980
$\mathbf{C}_{VV}$	0.997	0.992	0.997	0.997	0.997		0.998		0.998

Table 7. Values for AMSR2 $1 - \eta$ and AMSR2 V/H cross-polarization matrix elements $\mathbf{C}_{VV} = 1 - \mathbf{C}_{VH}$ and $\mathbf{C}_{VV} = \mathbf{C}_{HH}$.

Fig. 6 shows the size of the NL term ΔT_{NL} as function of TA for all AMSR2 channels. The amplitudes of the AMSR2 NL are significantly larger than for the other sensors. The AMSR2 values reach 1–3 K, whereas for WindSat the NL varies between 0.0 and 0.6 K (Table 6) and between 0.0 and 0.5 K for GMI (Wentz and Draper 2016). In addition, the AMSR2 NL terms differ for V-pol and H-pol at each band, and they can be positive or negative. We can also see from Fig. 6 that the quadratic fit, Equation (2), would be inaccurate for the AMSR2 NL term. As such, the higher order polynomial fit, Equation (3), is warranted.

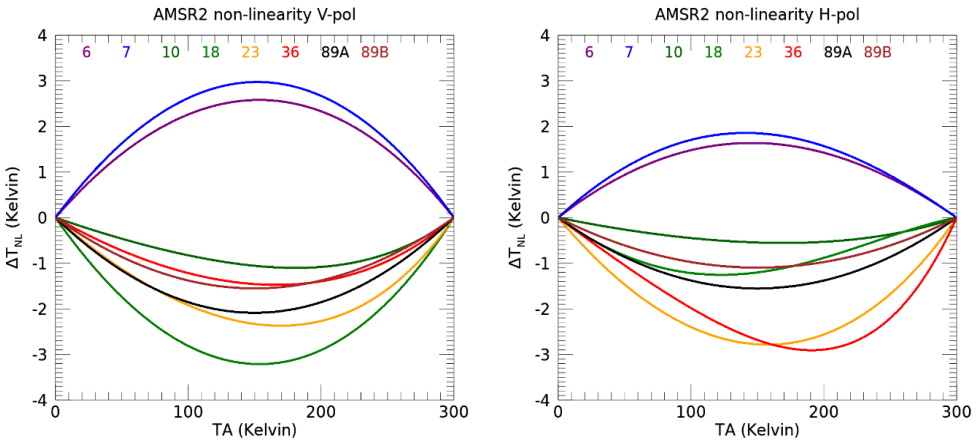

Fig. 6. Size of the NL terms ΔT_{NL} (Equation (3)) of the AMSR2 channels. Left: V-pol. Right H-pol.

568 *b. Center frequencies of AMSR2 18H and 23V passbands*

569 As indicated in Table 3, we use passband center frequencies for the 18H and 23V chan-
570 nels that differ from the nominal values in the AMSR2 absolute calibration. The 18H center
571 frequency is 100 MHz lower than the nominal value (18.7 GHz) and the 23V center fre-
572 quency is 70 MHz lower than the nominal value (23.8 GHz). The reason for doing this is that
573 using the nominal values for these channels would result in fits for the NL terms with very
574 unusual behaviors. The NL curves would switch sign over the dynamical TA range, which is
575 an unlikely scenario. We note that the 18.7 GHz and 23.8 GHz channels are in close proxim-
576 ity to the 22.234 GHz water vapor absorption resonance, which causes the atmospheric ab-
577 sorption coefficients, and thus the TOA TB, to be very sensitive to small changes in the chan-
578 nel frequencies. We have chosen to make small adjustments to the center frequencies rather
579 than using oddly shaped NL curves. Unlike WindSat, we have no detailed information about
580 the shape of the AMSR2 passband, which causes this ambiguity in the sensor calibration.

581 *c. TB over the open ocean*

582 Once the absolute calibration constants for WindSat and AMSR2 have been determined,
583 we can compare the intercalibrated sensor TB with the RTM TB. The results for the global
584 statistics over the open ocean are listed in Table 8 for WindSat and Table 9 for AMSR2.
585 From Table 8, it is apparent that the 10 and 18 GHz WindSat absolute biases are slightly
586 lower than for GMI, while at 37 GHz GMI performs better than WindSat (Table 4). AMSR2
587 exhibits the same pattern of performance relative to GMI (Table 9). Because of the large
588 AMSR2 NL term this result was not guaranteed. It indicates that our fits for the AMSR2 ΔT_{NL}
589 were done accurately. WindSat and AMSR2 absolute biases are within 0.42 K for the 10, 18
590 and 37 GHz bands.

591

Band	6	10	18	23	37
Bias	0.00	0.00	-0.09	-0.16	-0.20
Std.Dev.	0.19	0.23	0.26	0.29	0.30

592 Table 8. Global statistics for WindSat measured minus RTM TB over the open ocean us-
593 ing the combination $2V - H$ for the bias and $(2V - H)/\mathrm{sqrt}(5)$ for the standard deviation of the
594 error. All values are in Kelvin.

595

Band	6	7	10	18	23	36	89

Bias	+0.09	+0.07	-0.04	+0.09	-0.18	-0.42	-1.00
Std.Dev.	0.31	0.32	0.33	0.29	0.30	0.32	0.82

Table 9. Global statistics for AMSR2 measured minus RTM TB over the open ocean using the combination *2V – H* for the bias and (*2V – H*)/sqrt(*5*) for the standard deviation of the error. All values are in Kelvin.

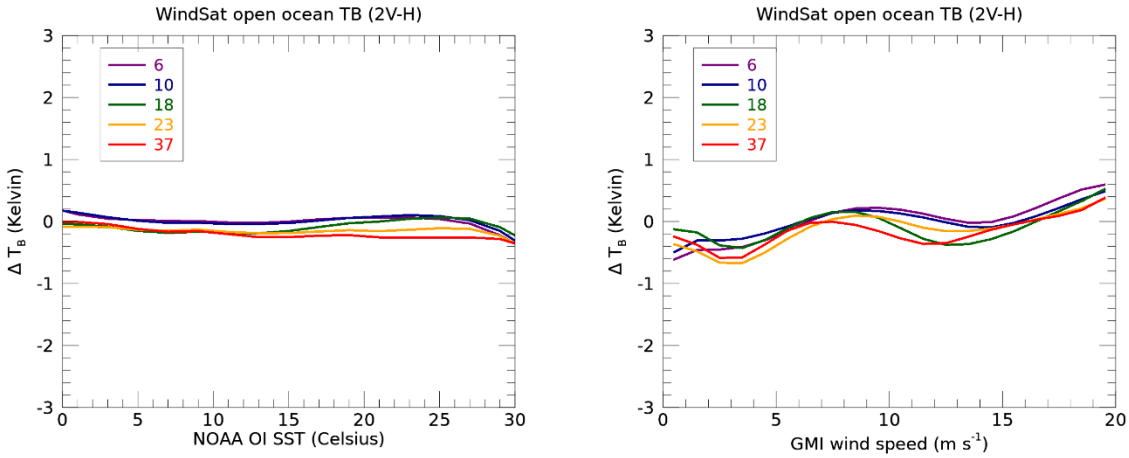

Fig. 7. Measured minus RTM TB *2V – H* over the open ocean for the WindSat bands (6, 10, 18, 23, 37 GHz) shown over a wide range of SSTs (left) and wind speeds (right).

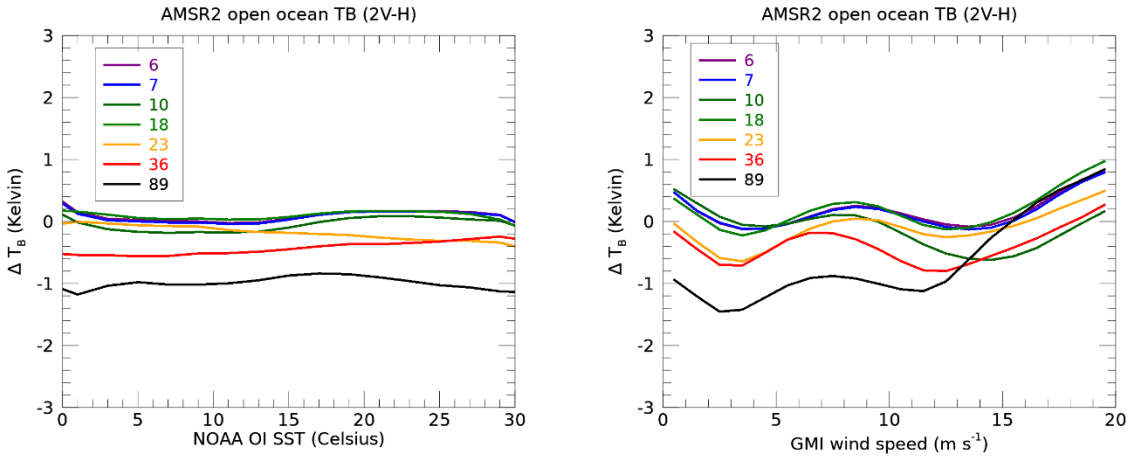

Fig. 8. Measured minus RTM TB *2V – H* over the open ocean for the AMSR2 bands (6, 7, 10, 18, 23, 36, 89 GHz) shown over a wide range of SSTs (left) and wind speeds (right).

The TB measured – RTM curves as functions of SST and wind speed are shown in Fig. 7 for WindSat and Fig. 8 for AMSR2. Note that the stratification with respect to wind speed in the right panel is done versus the GMI wind speed. These figures indicate that there are no significant cross-talk biases for WindSat or AMSR2. An exception to this is the AMSR2 89

GHz channel where somewhat larger deviations between measured TB and the RTM values are found, though they are still below 1.5 K. Similar to the GMI results, the undulating nature of the TB errors when binned by wind speed is likely a result of uncertainty in the RTM surface roughness model.

d. Wind speed and water vapor measurements over the open ocean

The next step in the open ocean intercalibration is a validation of the WindSat and AMSR2 wind speed and water vapor retrievals versus in-situ ground truth measurements. As we have done in the case of GMI (Section 3b), we compare the WindSat and AMSR2 wind speed retrievals with buoy observations and the water vapor retrievals with GPS observations. Fig. 9 and Fig. 10 show results for the WindSat and AMSR2 in-situ validation, respectively. WindSat's and AMSR2's wind speed RMSEs are 0.87 m s^{-1} and 0.84 m s^{-1}, respectively, and their water vapor RMSEs are 1.63 mm and 1.65 mm, respectively. These values are similar to the GMI values of 0.92 m s^{-1} and 1.64 mm. Because GMI, WindSat, and AMSR2 use the same retrieval algorithm, these similarities suggest that WindSat and AMSR2 TB have reached an absolute calibration accuracy similar to GMI TB.

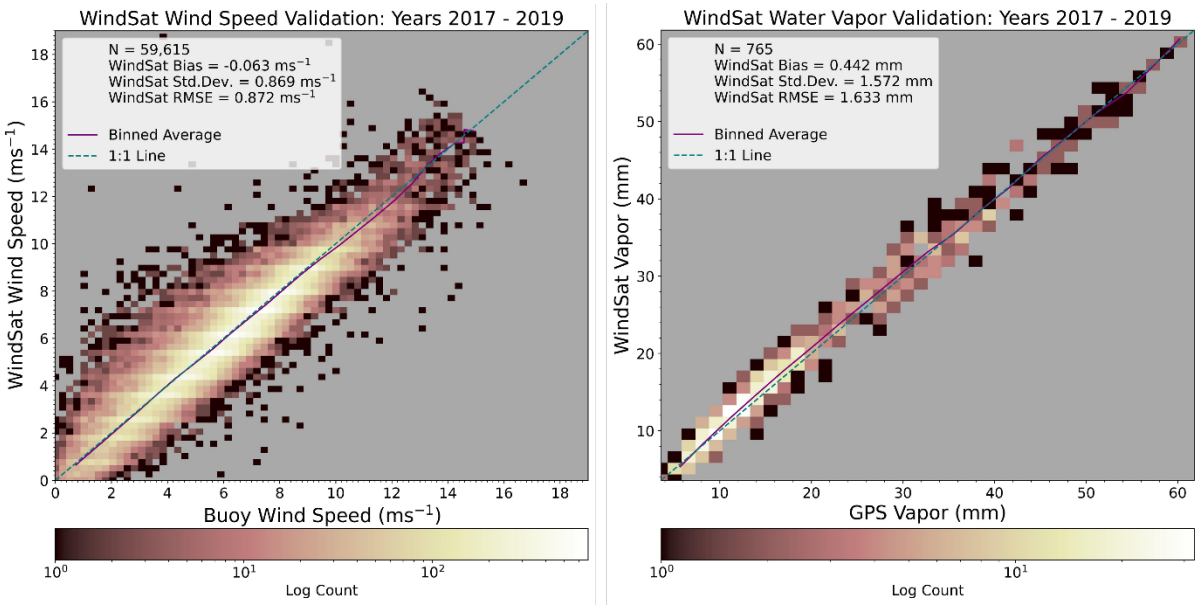

Fig. 9. Scatterplots of WindSat versus buoy wind speeds (left) and WindSat versus GPS columnar water vapor (right).

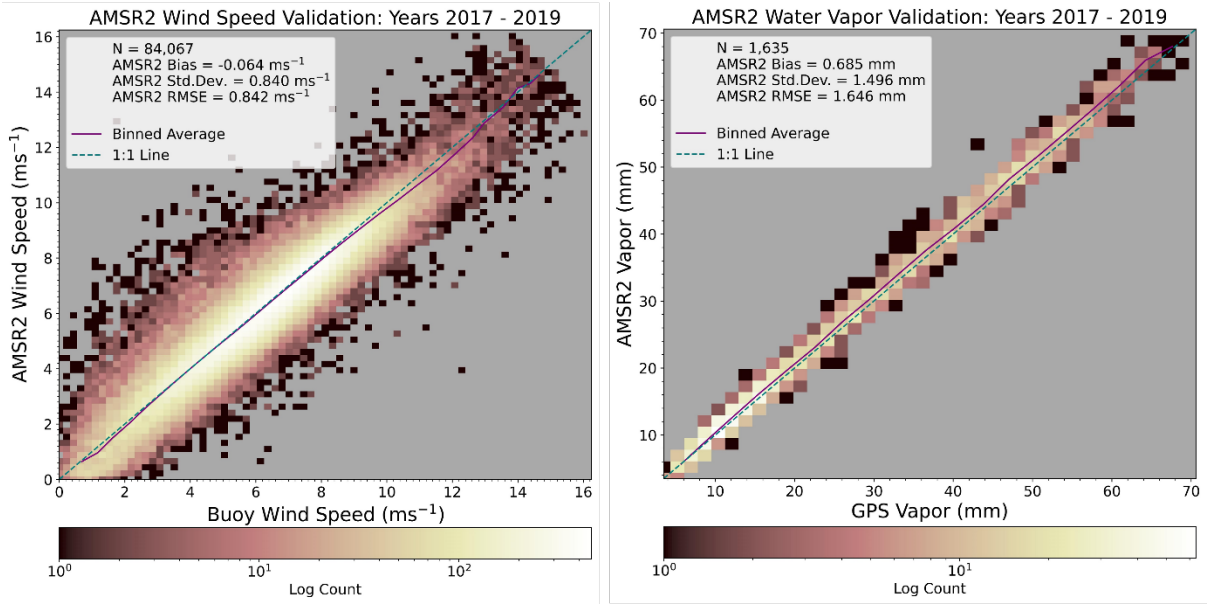

632

633 Fig. 10. Scatterplots of AMSR2 versus buoy wind speeds (left) and AMSR2 versus GPS
634 columnar water vapor (right).

635

636 *e. TB over the rainforest*

637 Table 10 and Table 11 show the overall statistics for TB measured – RTM for WindSat
638 and AMSR2 over the Amazon rainforest. We have separated the results into ascending (ASC,
639 local time ≈ 18:00 for WindSat and 13:30 for AMSR2) and descending (DSC, local time ≈
640 6:00 for WindSat and 1:30 for AMSR2) swaths in order to validate retrievals at different
641 points in the diurnal cycle. In the 10 and 18 GHz bands, WindSat's ASC absolute biases and
642 standard deviations are higher than the DSC values; however, the reverse is true for the 37
643 GHz band. Similarly, we find lower absolute bias and standard deviation values for the
644 AMSR2 DSC passes as compared to the AMSR2 ASC passes over the 10, 18, and 37 GHz
645 bands. The difference between the ASC and DSC passes is larger for AMSR2 than for Wind-
646 Sat. The WindSat and AMSR2 absolute biases over the Amazon rainforest are within 0.45 K
647 for 10, 18, and 37 GHz.

648

Swath	Local Time	Band	6	10	18	23	37
ASC	18:00	Bias	+0.02	+0.33	+0.32	+0.36	0.02
		Std.Dev.	1.23	1.24	1.04	0.86	1.11
DSC	6:00	Bias	+0.06	-0.16	-0.11	+0.06	-0.22
		Std.Dev.	1.01	1.14	1.03	0.77	1.05

649 Table 10. Statistics for WindSat measured minus RTM over the rainforest scene for
650 *(V+H)/2* TB. The results have been separated into ascending (ASC) and descending (DSC)
651 swaths. All values are in Kelvin.

652

Swath	Local Time	Band	6	7	10	18	23	36	89
ASC	13:30	Bias	-1.13	-1.15	-0.45	-0.42	-0.25	-0.33	-0.37
		Std.Dev.	1.66	1.67	1.66	1.47	1.15	1.37	1.79
DSC	1:30	Bias	+0.13	+0.05	+0.10	+0.06	+0.23	+0.12	-0.24
		Std.Dev.	1.02	1.04	1.08	0.96	0.74	0.94	1.60

653 Table 11. Statistics for AMSR2 measured minus RTM over the rainforest scene for
654 *(V+H)/2* TB. The results have been separated into ascending (ASC) and descending (DSC)
655 swaths. All values are in Kelvin.

656

657 Over the average diurnal cycle, the WindSat and AMSR2 TB in each pass agree very well
658 with the diurnal variation of the GMI TB (Fig. 5). This is expected, as the GMI and Wind-
659 Sat/AMSR2 TB have been matched to find the values of the WindSat and AMSR2 absolute
660 calibration parameters. An independent check of the TB over the rainforest scene can be ob-
661 tained by looking at their seasonal variation and how well it matches the RTM prediction
662 (Fig. 11, Fig. 12). Similar to the average statistics given in Table 10 and Table 11, we find
663 that the results for the descending night and early morning passes are slightly better than for
664 the ascending afternoon and early evening passes. This is likely caused by RTM error. More
665 specifically, the ERA5 ancillary fields for surface temperature and atmospheric profiles are
666 more accurate at the local early morning time than at the local early evening time when cloud
667 and rain cover are more likely.

668

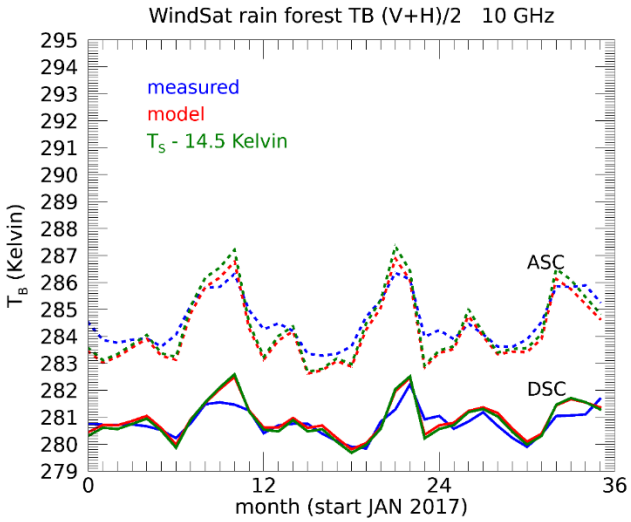

669

670 Fig. 11. Seasonal variation of the WindSat TB for 10 GHz *(V + H)/2* over the rainforest
671 scene. The curves show the measured TB (blue), the results of the RTM (red), and the varia-
672 tion of the surface temperature (green), which has been decreased by 14.5 K in order to align
673 with the measured and modeled TB. The results have been separated into ascending (ASC)
674 and descending (DSC) swaths.

675

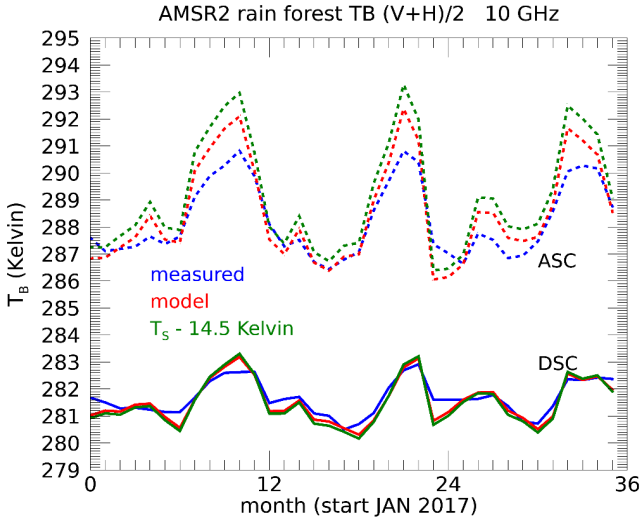

676

677 Fig. 12. Seasonal variation of the AMSR2 TB for 10 GHz *(V + H)/2* over the rainforest
678 scene. The curves show the measured TB (blue), the results of the RTM (red), and the varia-
679 tion of the surface temperature (green), which has been decreased by 14.5 K in order to align
680 with the measured and modeled TB. The results have been separated into ascending (ASC)
681 and descending (DSC) swaths.

682

6. Uncertainty assessment

The uncertainty values for TB measured – RTM listed in Table 4, Table 8, and Table 9 do not solely reflect the TB calibration uncertainty, but are composed of several contributions: (1) TB calibration uncertainty; (2) uncertainties in the RTM itself; (3) uncertainties in the ancillary input to the RTM computation including time mismatches between TB observations and the time stamp of the ancillary field; and (4) noise in the radiometer measurements (NEDT). The magnitude of the radiometer noise (4) after the OI resampling is performed is about 0.1 K. The uncertainties in the ancillary input parameters (3) can be estimated from a Monte-Carlo (MC) simulation that computes the RTM with and without typical RMS uncertainty estimates for ocean surface wind speed (0.8 m s^{-1}), SST (0.5 K), water vapor (1.5 mm), cloud liquid water (0.1 mm), and ocean surface wind direction (15°). The result of the MC simulation shows that the contribution of these uncertainties to the total budget is at least 0.2 K for the 6–37 GHz bands and at least 0.4 K for the 89 GHz bands. The estimates for the uncertainty sources (3) and (4) need to backed out in a root mean square sense from the standard deviations in Table 4, Table 8, and Table 9, which leaves us with an estimated uncertainty solely caused by sources (1) and (2). The resulting values for systematic (biases) and random (standard deviations) uncertainty estimates are summarized in Table 12 for the channels of the GMI – WindSat – AMSR2 intercalibration. We are not able to distinguish between uncertainty sources (1) and (2), so the values in Table 12 comprise both residual uncertainties in the absolute intercalibration and uncertainties in the ocean RTM.

We note that the values for the random components (standard deviations) of the uncertainty estimates given in Table 12 include errors associated with neglecting the dependence of ΔT_{NL} on the physical temperature of the receiver. We have neglected this temperature dependence in this study, as it adds another level of complexity and would thus exceed the scope of this paper. The values that are given in Table 7, Fig. 6 and Table 13 are all averages. A detailed analysis of the dependence of ΔT_{NL} on the receiver temperature for AMSR2 was performed by Wentz (2021).

Band	10		18		36 / 37		89	
	sys	ran	sys	ran	sys	ran	sys	ran
GMI	+0.09	0.23	+0.31	0.13	-0.02	0.05	+0.22	0.27

WindSat	0.00	0.05	-0.09	0.13	-0.20	0.20	N/A	
AMSR2	-0.04	0.24	+0.09	0.18	-0.42	0.23	-1.00	0.69

Table 12. Estimated systematic (sys) and random (ran) uncertainties of the intercalibrated GMI – WindSat – AMSR2 TB measured – RTM for open ocean scenes using the combination $2V - H$ for the systematic bias and $(2V - H)/\mathrm{sqrt}(5)$ for the random standard deviation of the error. All values are in Kelvin.

In regards to the Amazon rainforest TB, a comparison of land surface temperature measurements made by the infrared MODIS sensor with in-situ data shows an RMSE of about 1.5 K (Gomis-Cebolla et al. 2018). We can assume that the RMSE of the ERA5 surface temperatures are at least as large. That means that the values for the standard deviations for TB measured – RTM over the rainforest for GMI (Table 5), WindSat (Table 10), and AMSR2 (Table 11) are largely if not entirely caused by errors in the ancillary surface temperature input and not by the errors in the intercalibration.

7. Discussion and Conclusions

We have performed an on-orbit intercalibration of WindSat and AMSR2 to GMI over the open ocean and the Amazon rainforest. The absolute calibration of the TOA TB of these sensors consists of determining the values for antenna spillover, antenna cross-polarization, and receiver non-linearity. An accurate knowledge of these parameters will result in accurately calibrated TB over a wide dynamical range comprising ocean, ice, and land scenes. The sensor intercalibration methodology does not depend on a specific RTM because the RTM is only used for a minor adjustment to GMI TB. When compared to the RTM, the intercalibrated TOA TB absolute biases (standard deviations) range from 0.00 – 0.42 K (0.05 – 0.24 K) and the RMSE is within 0.5 K for the 10, 18, and 37 GHz channels. Wind speed and water vapor retrievals from all three satellite sensors were validated versus in-situ measurements and show comparable levels of accuracy, i.e., a wind speed RMSE of 0.84 – 0.92 m s^{-1} and a water vapor RMSE of 1.63 – 1.65 mm for GMI, WindSat, and AMSR2. The biases between the intercalibrated TB and the rainforest RTM range from 0.01 – 0.45 K for the 10, 18, and 37 GHz channels. The standard deviations for the rainforest RTM TB difference are largely governed by the ERA5 surface temperature input.

We want to mention that an accurate on-orbit calibration for any microwave radiometer requires more than determining the absolute calibration parameters. It includes, for instance,

(1) correction of sensor pointing errors; (2) correction of Earth, moon, or RFI radiation into the cold sky mirror; (3) correction of along-scan biases that can be caused by intrusion of the spacecraft or calibration loads into the Earth field of view; (4) correction of sun intrusion into the hot calibration load; (5) correction for a finite emissivity of the reflector antenna; (6) corrections for temporal drifts in the noise-diode injection temperatures or receiver non-linearities; (7) calibration of the polarimetric channels; (8) magnetic field sensitivity errors. All known passive microwave sensors have experienced at least some of these problems to a certain extent. A comprehensive discussion of many of these issues was given in Meissner et al. (2012).

The WindSat and AMSR2 TOA TB that have been absolutely intercalibrated to GMI differ significantly from TB that are obtained if pre-launch measurements of spillover, cross-polarization and non-linearities are used in the sensor calibration. Depending on the channel, AMSR2 TB based on pre-launch calibration parameters (JAXA, 2012b) are on average about 2.0 – 4.5 K higher over the open ocean and about 0.5 – 1.5 K higher over the rainforest scenes than the ones intercalibrated to GMI. WindSat TB based on pre-launch calibration parameters (M. H. Bettenhausen, 2006, personal communication) are on average about 1 – 2 K higher over the open ocean and about 3 K over the rainforest scenes than the ones intercalibrated to GMI. It follows that the TOA TB that are based on pre-launch calibration parameters cannot be used directly in a physically-based ocean retrieval algorithm for W and V like it was used in our study (Section 3b). Doing so would result in large biases for the ocean retrievals. These TOA TB could be used directly either in purely statistical regressions or machine-learning algorithms that do not use a physical RTM. In order to use them in a physically based retrieval it will be necessary to re-calibrate them over ocean targets to a specific RTM. However, the resulting TOA TB will then depend on the specific RTM that has been chosen and it is required to use this same RTM in both calibration and retrieval. As we have pointed out (Section 4e) the TOA TB intercalibration does not depend significantly on the choice of the RTM. As a matter of fact, the absolutely intercalibrated TOA TB can actually be used to assess the quality of different RTMs from the literature by comparing the biases between intercalibrated TB and RTM computed TB, which should be small. That gives the absolutely intercalibrated TB a clear advantage over the TB that are based on pre-launch calibration parameters.

Once the absolute intercalibration for WindSat/AMSR2 to GMI has been performed and validated, these sensors themselves can serve as absolute calibration references for the

channels of other passive sensors that overlap in time. In order to avoid the accumulation of systematic errors from one sensor to the next, each intercalibrated sensor will need to be assessed with the RTM and in-situ data similar to the validation procedures given in this paper. In the past, these other passive sensors included TMI, AMSR-E, and the series of SSM/I and SSMIS going back to the first SSM/I that was launched in 1987. Going forward, we can include the U.S. Airforce Compact Ocean Wind Vector Radiometer (COWVR) that was launched in 2021 (Brown et al. 2017), the JAXA AMSR3 onboard GOSAT-GW that is scheduled to launch in 2024 (Kachi et al. 2023), the U.S. DoD Weather System Follow on MicroWave Imager (WSF-M MWI) launched in 2024 (Draper et al. 2023; Lindsley et al. 2023), the EUMETSAT 2nd generation Microwave Imager (MWI) that is scheduled to launch in 2026 (Lupi et al. 2020), and, ultimately, the ESA Copernicus Imaging Microwave Radiometer (CIMR), that is anticipated to launch in or after 2029 (Donlon et al. 2023). The successive intercalibration of these radiometers will enable the creation of a consistent long-term climate data record.

Acknowledgments.

This research was funded in part under NASA ROSES grant 80NSSC21K0545 (USPI: Development of Ocean Retrieval Algorithms for the Copernicus Imaging Microwave Radiometer). We would like to thank Peter Gaiser (Naval Research Laboratory, Washington, DC) for providing us with WindSat L1A data and the JAXA G-portal team for providing us with AMSR2 L1A data. GMI data comes from the NASA Goddard Space Flight Center.

Data Availability Statement.

The daily 0.25° gridded ascending and descending TB maps for GMI, WindSat, and AMSR2 are publicly available at https://images.remss.com/~RSS-TB/intercalibration/ as netCDF files. The maps include quality control flags, all of the ancillary fields that are required in the RTM computation, and the satellite retrievals for W, V, and L.

Fortran90 code for the ocean surface emissivity RTM is publicly available at https://github.com/Remote-Sensing-Systems/RSS-Ocean-Surface-Emissivity-Model.

APPENDIX A

Updated Model for Atmospheric Water Vapor Absorption

This appendix briefly summarizes the small updates and adjustment that have been made to the water vapor absorption model of Wentz and Meissner (2016).

1. The half-width γ of the air-broadened 22.234 GHz water vapor line has been reduced by 4%.

2. The scaling factor 1.01 in Equation (1) of Wentz and Meissner (2016) has been rescinded. That means that $S' = S$.

3. The wings of the 22.234 GHz water vapor line have been adjusted. Equation (13) in Wentz and Meissner (2016) has been changed to:

$$\chi = 0.07 \cdot \gamma + 0.93 \cdot \gamma \cdot x^2 \cdot (3 - 2x)$$

$$x = \begin{cases} \dfrac{19 - f}{16.5} & 2.5 \le f \le 19 \\ 0 & f > 19 \\ 1 & f < 2.5 \end{cases}, \tag{11}$$

where f denotes the frequency in GHz.

4. The half-width γ of the air-broadened 183.81 GHz water vapor line has been increased by 3%.

5. For the foreign-broadened (FB) water vapor continuum we use the expression given by Rosenkranz (2017).

6. For the self-broadened (SB) water vapor continuum we use the expression given by Rosenkranz (2017) reduced by 7%.

These changes and adjustments were based on recent analysis of satellite observations. They also bring the water vapor absorption coefficients into better agreement with the recent literature (Liljegren et al. 2005; Payne et al. 2008; Rosenkranz 2017).

APPENDIX B

Values for the AMSR2 Non-Linearity Coefficients

For reference, we list the numerical values of the AMSR2 NL coefficients $a_{NL,i}$ that are used in Equation (3) for computing ΔT_{NL} in Table 13.

channel	$a_{NL,1}$	$a_{NL,2}$	$a_{NL,3}$	$a_{NL,4}$	$a_{NL,5}$
6V	-9.986E+00	9.569E+00	6.637E-02	1.425E-01	2.079E-01
6H	-6.811E+00	7.174E+00	-8.310E-02	-1.300E-01	-1.499E-01
7V	-1.166E+01	1.136E+01	4.666E-02	1.009E-01	1.479E-01
7H	-8.049E+00	8.929E+00	-2.008E-01	-3.150E-01	-3.637E-01
10V	3.031E+00	-1.491E+00	-2.432E-01	-5.256E-01	-7.719E-01
10H	1.788E+00	-1.263E+00	-1.135E-01	-1.877E-01	-2.240E-01
18V	1.240E+01	-1.185E+01	-8.044E-02	-1.852E-01	-2.871E-01
18H	6.378E+00	-8.447E+00	3.917E-01	7.288E-01	9.489E-01
23V	7.710E+00	-5.649E+00	-2.860E-01	-6.822E-01	-1.093E+00
23H	1.039E+01	-9.538E+00	-1.884E-03	-2.050E-01	-6.444E-01
36V	4.994E+00	-3.938E+00	-1.285E-01	-3.373E-01	-5.899E-01
36H	6.462E+00	-9.237E-01	-9.138E-01	-1.907E+00	-2.717E+00
89AV	8.342E+00	-8.342E+00	0.000E+00	0.000E+00	0.000E+00
89AH	6.206E+00	-6.206E+00	0.000E+00	0.000E+00	0.000E+00
89BV	6.203E+00	-6.203E+00	0.000E+00	0.000E+00	0.000E+00
89BH	4.383E+00	-4.383E+00	0.000E+00	0.000E+00	0.000E+00

Table 13. Values of the NL coefficients $a_{NL,i}$, $i=1,\ldots5$ of the AMSR2 channels. All values are in Kelvin.

REFERENCES

Ashcroft, P. D., and F. J. Wentz, 2000: AMSR Level 2A Algorithm, report number 121599B-1, Remote Sensing Systems, Santa Rosa, CA, 29 pp, https://doi.org/10.56236/RSS-ag.

Bell, W., and Coauthors, 2008: The Assimilation of SSMIS Radiances in Numerical Weather Prediction Models. *IEEE Trans. Geosci. Remote Sens.*, **46**, 884–900, https://doi.org/10.1109/TGRS.2008.917335.

Bettenhausen, M. H., and P. W. Gaiser, 2014: Analysis of the WindSat Receiver Frequency Passbands, report number NRL/MR/7220--14-9558, Naval Research Laboratory, Washington, DC, 13 pp, https://apps.dtic.mil/sti/pdfs/ADA610946.pdf.

Biswas, S. K., S. Farrar, K. Gopalan, A. Santos-Garcia, W. L. Jones, and S. Bilanow, 2013: Intercalibration of Microwave Radiometer Brightness Temperatures for the Global Precipitation Measurement Mission. *IEEE Trans. Geosci. Remote Sens.*, **51**, 1465–1477, https://doi.org/10.1109/TGRS.2012.2217148.

Blewitt, G., W. C. Hammond, and C. Kreemer, 2018: Harnessing the GPS data explosion for interdisciplinary science. *Eos,* **99**, https://doi.org/10.1029/2018EO104623.

Bourlès, B., and Coauthors, 2008: THE PIRATA PROGRAM. *Bull. Amer. Meteor. Soc.*, **89**, 1111–1126, https://doi.org/10.1175/2008BAMS2462.1.

Brown, S., and C. S. Ruf, 2005: Determination of an Amazon Hot Reference Target for the On-Orbit Calibration of Microwave Radiometers. *J. Atmos. Oceanic Technol.*, **22**, 1340–1352, https://doi.org/10.1175/JTECH1769.1.

Brown, S., and Coauthors, 2017: The COWVR Mission: Demonstrating the capability of a new generation of small satellite weather sensors. *2017 IEEE Aerospace Conference*, Big Sky, MT, USA, 1–7, https://doi.org/10.1109/AERO.2017.7943884.

Colton, M. C., and G. A. Poe, 1999: Intersensor calibration of DMSP SSM/I's: F-8 to F-14, 1987-1997. *IEEE Trans. Geosci. Remote Sens.*, **37**, 418–439, https://doi.org/10.1109/36.739079.

DFO, 2023: Marine Environmental Data Section Archive, Ecosystem and Oceans Science, Department of Fisheries and Oceans Canada, accessed 4 December 2023, https://meds-sdmm.dfo-mpo.gc.ca.

Donlon. C., and Coauthors, 2023: The Copernicus Imaging Microwave Radiometer (CIMR): Mission Overview and Status. *2023 IEEE International Geoscience and Remote Sensing Symposium*, Pasadena, CA, USA, 989–992, https://doi.org/10.1109/IGARSS52108.2023.10281934.

Draper, D., D. A. Newell, F. J. Wentz, S. Krimchansky, and G. Skofronick-Jackson, 2015a: The Global Precipitation Measurement (GPM) Microwave Imager (GMI): Instrument overview and early on-orbit performance. *IEEE J. Sel. Top. Appl. Earth Obs. Remote Sens.*, **8**, 3452–3462, https://doi.org/10.1109/JSTARS.2015.2403303.

Draper, D. W., D. A. Newell, D. S. McKague, and J. R. Piepmeier, 2015b: Assessing Calibration Stability Using the Global Precipitation Measurement (GPM) Microwave Imager

(GMI) Noise Diodes, *IEEE J. Sel. Top. Appl. Earth Obs. Remote Sens*, **8**, 4239–4247, https://doi.org/10.1109/JSTARS.2015.2406661.

Draper, D., M. Berberich, Q. Remund, and F. Wentz, 2023: Calibration of the Fully Polarimetric Microwave Imager (MWI) on the Weather System Follow-on – Microwave (WSF-M) Satellite. *2023 IEEE International Geoscience and Remote Sensing Symposium*, Pasadena, CA, USA, 475–478, https://doi.org/10.1109/IGARSS52108.2023.10281428.

ECMWF, 2019: ECMWF Reanalysis v5 (ERA5), accessed 4 December 2023, https://www.ecmwf.int/en/forecasts/dataset/ecmwf-reanalysis-v5.

Gaiser. P. W., and Coauthors, 2004: The WindSat spaceborne polarimetric microwave radiometer: sensor description and early orbit performance. *IEEE Trans. Geosci. Remote Sens.*, **42**, 2347–2361, https://doi.org/10.1109/TGRS.2004.836867.

Gomis-Cebolla, J., J. C. Jimenez, and J. A. Sobrino, 2018: LST retrieval algorithm adapted to the Amazon evergreen forests using MODIS data. *Remote Sens. Environ.,* **204,** 401–411, https://doi.org/10.1016/j.rse.2017.10.015.

Gower, J. F. R., 2002: Temperature, Wind and Wave Climatologies, and Trends from Marine Meteorological Buoys in the Northeast Pacific. *J. Climate*, **15**, 3709–3718, https://doi.org/10.1175/1520-0442(2002)015<3709:TWAWCA>2.0.CO;2.

GPM Science Team, 2022: GPM GMI RSS Common Calibrated Brightness Temperatures L1BASE 1.5 hours 13 km V07, Greenbelt, MD, USA, NASA Goddard Earth Science Data and Information Services Center (GES DISC), accessed 4 December 2023, https://doi.org/10.5067/GPM/GMI/BASE-RSS/07.

Hollinger, J. P., J. L. Peirce and G. A. Poe, 1990: SSM/I instrument evaluation. *IEEE Trans. Geosci. Remote Sens.,* **28**, 781–790, https://doi.org/10.1109/36.58964.

Huang, B., C. Liu, V. Banzon, E. Freeman, G. Graham, B. Hankins, T. Smith, and H.-M. Zhang, 2021: Improvements of the Daily Optimum Interpolation Sea Surface Temperature (DOISST) Version 2.1. *Journal of Climate*, **34**, 2923–2939, https://doi.org/10.1175/JCLI-D-20-0166.1.

Huffman, G. J., E. F. Stocker, D. T. Bolvin, E. J. Nelkin, and Jackson Tan, 2019: GPM IMERG Final Precipitation L3 Half Hourly 0.1° x 0.1° V06, Greenbelt, MD, Goddard Earth Sciences Data and Information Services Center (GES DISC), accessed 4 December 2023, https://doi.org/10.5067/GPM/IMERG/3B-HH/06.

HYCOM, 2014: Hybrid Coordinate Ocean Model, Global Ocean Forecasting System (GOFS) 3.1 output on the GLBy0.08 grid, Top layer salinity, accessed 4 December 2023, www.hycom.org.

JAXA, 2012a: GCOM-W/AMSR2 L1A data, accessed 4 December 2023, https://gportal.jaxa.jp/gpr/?lang=en (provided upon special request).

JAXA, 2012b: GCOM-W/AMSR2 L1B data, accessed 4 December 2023, https://gportal.jaxa.jp/gpr/?lang=en.

Kachi, M. et al. 2023: The Advanced Microwave Scanning Radiometer 3 (AMSR3) Onboard the Global Observing Satellite for Greenhouse Gases and Water Cycle (GOSAT-GW) Toward Long-Term Water Cycle Monitoring, *2023 IEEE International Geoscience and Remote Sensing Symposium*, Pasadena, CA, USA, 561–564, https://doi.org/10.1109/IGARSS52108.2023.10282052.

Kawanishi, T., and Coauthors, 2003: The Advanced Microwave Scanning Radiometer for the Earth Observing System (AMSR-E), NASDA's contribution to the EOS for global energy and water cycle studies. *IEEE Trans. Geosci. Remote Sens.,* **41**, 184–194, https://doi.org/10.1109/TGRS.2002.808331.

Kroodsma, R. A., D. S. McKague, and C. S. Ruf, 2012: Inter-Calibration of Microwave Radiometers Using the Vicarious Cold Calibration Double Difference Method. *IEEE J. Sel. Top. Appl. Earth Obs. Remote Sens.*, **5**, 1006–1013, https://doi.org/10.1109/JSTARS.2012.2195773.

Kummerow, C., and Coauthors, 2000: The Status of the Tropical Rainfall Measuring Mission (TRMM) after Two Years in Orbit. *J. Appl. Meteor. Climatol.*, **39**, 1965–1982, https://doi.org/10.1175/1520-0450(2001)040<1965:TSOTTR>2.0.CO;2.

Kunkee, D. B., and Coauthors, 2008: Design and Evaluation of the First Special Sensor Microwave Imager/Sounder. *IEEE Trans. Geosci. Remote Sens.,* **46**, 863–883, https://doi.org/10.1109/TGRS.2008.917980.

Liljegren, J. C. S. -A. Boukabara, K. Cady-Pereira, and S. A. Clough, 2005: The effect of the half-width of the 22-GHz water vapor line on retrievals of temperature and water vapor profiles with a 12-channel microwave radiometer. *IEEE Trans. Geosci. Remote Sens.,* **43**, 1102–1108, https://doi.org/10.1109/TGRS.2004.839593.

Lindsley, R. D., F. J. Wentz, D. W. Draper, K. Shahady, and B. Ellis, 2023: WSF-M On-orbit CAL/VAL Techniques. *2023 IEEE International Geoscience and Remote Sensing Symposium*, Pasadena, CA, USA, 479–482, https://doi.org/10.1109/IGARSS52108.2023.10281995.

Lupi, T., and Coauthors, 2020: MicroWave Imager for MetOp-SG: development status and Instrument verification. *2020 16th Specialist Meeting on Microwave Radiometry and Remote Sensing for the Environment (MicroRad)*, Florence, Italy, 1–4, https://doi.org/10.1109/MicroRad49612.2020.9342547.

Mears, C. A., D. K. Smith, and F. J. Wentz, 2001: Comparison of Special Sensor Microwave Imager and buoy-measured wind speeds from 1987 to 1997, *J. Geophys. Res.*, **106** (C6), 11719–11729, https://doi.org/10.1029/1999JC000097.

Mears, C. A., J. Wang J., D. K. Smith, and F. J. Wentz, 2015: Intercomparison of total precipitable water measurements made by satellite-borne microwave radiometers and ground-based GPS instruments. *J. Geophys. Res. Atmos.*, **120**, 2492–2504, https://doi.org/10.1002/2014JD022694.

Meissner, T., and F. J. Wentz, 2002: An updated analysis of the ocean surface wind direction signal in passive microwave brightness temperatures. *IEEE Trans. Geosci. Remote Sens.*, **40**, 1230–1240, https://doi.org/10.1109/TGRS.2002.800231.

Meissner, T., and F. J. Wentz, 2004: The complex dielectric constant of pure and sea water from microwave satellite observations. *IEEE Trans. Geosci. Remote Sens.*, **42**, 1836–1849, https://doi.org/10.1109/TGRS.2004.831888.

Meissner, T., and F. J. Wentz, 2006a: Polarization rotation and the third Stokes parameter: the effects of spacecraft attitude and Faraday rotation. *IEEE Trans. Geosci. Remote Sens.*, **44**, 506–515, https://doi.org/10.1109/TGRS.2005.858413.

Meissner, T., and F. J. Wentz, 2006b: Ocean Retrievals for WindSat. *2006 IEEE MicroRad*, San Juan, PR, USA, 119–124, https://doi.org/10.1109/MICRAD.2006.1677074.

Meissner, T., and F. J. Wentz, 2010: Intercalibration of AMSR-E and WindSat brightness temperature measurements over land scenes. *2010 IEEE International Geoscience and Remote Sensing Symposium*, Honolulu, HI, USA, 3218–3219, https://doi.org/10.1109/IGARSS.2010.5649513.

964 Meissner, T., and F. J. Wentz, 2012: The emissivity of the ocean surface between 6 and 90
965 GHz over a large range of wind speeds and Earth incidence angles. *IEEE Trans. Geosci.*
966 *Remote Sens.*, **50**, 3004–3026, https://doi.org/10.1109/TGRS.2011.2179662.

967 Meissner, T., F. J. Wentz, and D. Draper, 2012: GMI Calibration Algorithm and Analysis
968 Theoretical Basis Document, report number 041912, Version-G, Remote Sensing Sys-
969 tems, Santa Rosa, CA, 124 pp, https://doi.org/doi.org/10.56236/RSS-au.

970 Meissner, T., F. J. Wentz, and L. Ricciardulli, 2014: The emission and scattering of L-band
971 microwave radiation from rough ocean surfaces and wind speed measurements from the
972 Aquarius sensor. *J. Geophys. Res. Oceans*, **119**, 6499–6522, https://doi.org/
973 10.1002/2014JC009837.

974 Meissner, T., F. Wentz, and M. Brewer, 2022: RSS WindSat L1C TOA Brightness Tempera-
975 tures, V08.0, accessed 16 December 2023, https://doi.org/10.5067/WSA80-1CRTB.

976 Meissner, T., K. Wentz and F. Wentz, 2023: RSS AMSR2 TB on daily 0.25 grid, Version
977 8.2, Remote Sensing Systems, Santa Rosa, CA, accessed 16 December 2023,
978 https://doi.org/10.56236/RSS-bk.

979 Mo, T., 2007: Diurnal variation of the AMSU-A brightness temperatures over the Amazon
980 rainforest. *IEEE Trans. Geosci. Remote Sens.*, **45**, 958–969,
981 https://doi.org/10.1109/TGRS.2006.890417.

982 McPhaden, M. J., and Coauthors, 1998: The Tropical Ocean-Global Atmosphere observing
983 system: A decade of progress, *J. Geophys. Res.*, **103** (C7), 14169–14240,
984 https://doi.org/10.1029/97JC02906.

985 McPhaden, M. J., and Coauthors, 2009: RAMA: The Research Moored Array for African–
986 Asian–Australian Monsoon Analysis and Prediction. *Bull. Amer. Meteor. Soc.*, **90**, 459–
987 480, https://doi.org/10.1175/2008BAMS2608.1.

988 NDBC, 2023: National Data Buy Center web site and data archive, accessed 4 December
989 2023, https://www.ndbc.noaa.gov/.

990 NGL, 2023: Nevada Geodetic Laboratory GPS data, Stations DGAR, J497, J603, J743, J746,
991 MAC1, MCIL, SNI1, XMIS, accessed 4 December 2023, http://geod-
992 esy.unr.edu/NGLStationPages/GlobalStationList.]

993 Njoku, E. G., and L. Li, 1999: Retrieval of land surface parameters using passive microwave
994 measurements at 6-18 GHz. *IEEE Trans. Geosci. Remote Sens.,* **37**, 79–93,
995 https://doi.org/10.1109/36.739125.

996 NOAA, 2020, OI SST V2.1 High Resolution Dataset, accessed 4 December 2023,
997 https://psl.noaa.gov/data/gridded/data.noaa.oisst.v2.highres.html.

998 Oki, T., K. Imaoka, and M. Kachi, 2010: AMSR instruments on GCOM-W1/2: Concepts and
999 applications. *2010 IEEE International Geoscience and Remote Sensing Symposium*, Hon-
1000 olulu, HI, USA, 1363–1366 , https://doi.org/10.1109/IGARSS.2010.5650001.

1001 Payne, V. H., and Coauthors, 2008: Air-Broadened Half-Widths of the 22- and 183-GHz Wa-
1002 ter-Vapor Lines. *IEEE Trans. Geosci. Remote Sens.,* **46**, 3601–3617,
1003 https://doi.org/10.1109/TGRS.2008.2002435.

1004 Piepmeier, J., D. Long, and E. Njoku, 2008: Stokes antenna temperatures. *IEEE Trans. Ge-*
1005 *osci. Remote Sens.,* **46**, 516–527, https://doi.org/10.1109/TGRS.2007.909597.

1006 PMEL, 2023: Global Tropical Moored Buoy Array, accessed 4 December 2023,
1007 https://www.pmel.noaa.gov/gtmba/mission.

1008 Poe, G. A., 1990: Optimum interpolation of imaging microwave radiometer data. *IEEE*
1009 *Trans. Geosci. Remote Sens.,* **28**, 800–810 , https://doi.org/10.1109/36.58966.

1010 Portmann, H., 2009: Handbook of automated data quality control checks and procedures. Na-
1011 tional Data Buoy Center Tech. Doc. 09-02, 78 pp,
1012 http://www.ndbc.noaa.gov/NDBCHandbookofAutomatedDataQualityControl2009.pdf.

1013 Reynolds, R. W., N. A. Rayner, T. M. Smith, D. C. Stokes, and W. Wang, 2002: An im-
1014 proved in situ and satellite SST analysis for climate. *J. Climate*, **15**, 1609–1625,
1015 https://doi.org/10.1175/1520-0442(2002)015,1609:AIISAS.2.0.CO;2.

1016 Rosenkranz, P. W., 2017: Line-by-line microwave radiative transfer (non-scattering).
1017 FORTRAN code, Remote Sensing Code Library, accessed 4 December 2023, doi:
1018 10.21982/M81013, https://rscl-grss.org/.

1019 Sapiano, M. R. P., W. K. Berg, D. S. McKague, and C. D. Kummerow, 2013: Toward an In-
1020 tercalibrated Fundamental Climate Data Record of the SSM/I Sensors. *IEEE Trans. Ge-*
1021 *osci. Remote Sens.*, **51**, 1492–1503, https://doi.org/10.1109/TGRS.2012.2206601.

Twarog, E., W. E. Purdy, P. W. Gaiser, K. H. Cheung, and B. E. Kelm, 2006: WindSat on-orbit warm load calibration. *IEEE Trans. Geosci. Remote Sens.*, **44**, 516–529, https://doi.org/10.1109/TGRS.2005.863300.

Wentz, F. J., 1997: A well-calibrated ocean algorithm for special sensor microwave / imager. *J. Geophys. Res.*, **102**(C4), 8703–8718, https://doi.org/10.1029/96JC01751.

Wentz, F. J., and T. Meissner, 2000: AMSR-E Ocean Algorithm, Version 2; report number 121599A-1, Remote Sensing Systems, Santa Rosa, CA, 66 pp, https://doi.org/10.56236/RSS-af.

Wentz, F. J., P. Ashcroft, and C. Gentemann, 2001: Post-launch calibration of the TRMM microwave imager. *IEEE Trans. Geosci. Remote Sens.,* **39**, 415–422, https://doi.org/10.1109/36.905249.

Wentz, F. J., and T. Meissner, 2007: AMSR-E Ocean Algorithms; Supplement 1, report number 051707, Remote Sensing Systems, Santa Rosa, CA, 6 pp, https://doi.org/10.56236/RSS-am.

Wentz, F. J., 2013: SSM/I Version-7 Calibration Report, report number 011012, Remote Sensing Systems, Santa Rosa, CA, 46 pp, https://doi.org/10.56236/RSS-av.

Wentz, F.J., L. Ricciardulli, C. Gentemann, T. Meissner, K.A. Hilburn, J. Scott, 2013: Remote Sensing Systems Coriolis WindSat Daily Environmental Suite on 0.25 deg grid, Version 8.0, wind speed, columnar water vapor. Remote Sensing Systems, Santa Rosa, CA. Available online at www.remss.com/missions/windsat. Accessed October 2023.

Wentz, F. J., T. Meissner, C. Gentemann, K.A. Hilburn, J. Scott, 2014: Remote Sensing Systems GCOM-W1 AMSR2 Daily Environmental Suite on 0.25 deg grid, Version 8.2, wind speed, columnar water vapor. Remote Sensing Systems, Santa Rosa, CA. Available online at www.remss.com/missions/amsr. Accessed October 2023.

Wentz, F. J., 2015: A 17-Yr Climate Record of Environmental Parameters Derived from the Tropical Rainfall Measuring Mission (TRMM) Microwave Imager. *J. Climate*, **28**, 6882–6902, https://doi.org/10.1175/JCLI-D-15-0155.1.

Wentz, F. J., T. Meissner, J. Scott, and K.A. Hilburn, 2015: Remote Sensing Systems GPM GMI Air-Sea Essential Climate Variables, daily, on 0.25° grid, Version 8.2, wind speed, columnar water vapor, columnar cloud liquid water, rain rate, SST. Remote Sensing Systems, Santa Rosa, CA, accessed 4 December 2023, www.remss.com/missions/gmi.

Wentz, F. J., and D. Draper, 2016: On-Orbit Absolute Calibration of the Global Precipitation Measurement Microwave Imager. *J. Atmos. Oceanic Technol.*, **33**, 1393–1412, https://doi.org/10.1175/JTECH-D-15-0212.1.

Wentz, F. J., and T. Meissner, 2016: Atmospheric absorption model for dry air and water vapor at microwave frequencies below 100 GHz derived from spaceborne radiometer observations. *Radio Sci.*, **51**, 381–391, https://doi.org/10.1002/2015RS005858.

Wentz, F. J., 2021: AMSR-2 Air-Sea Essential Climate Variables, RSS Version 8.2, report number 05112021, Remote Sensing Systems, Santa Rosa, CA, 21 pp, accessed 20 July 2024, https://images.remss.com/papers/tech_reports/2021/AMSR-2_Air-Sea_Essential_Climate_Variables_RSS_Version_8.2.pdf.

Yang, J. X., D. S. McKague, and C. S. Ruf, 2016: Boreal, Temperate, and Tropical Forests as Vicarious Calibration Sites for Spaceborne Microwave Radiometry. *IEEE Trans. Geosci. Remote Sens.*, **54**, 1035–1051, https://doi.org/10.1109/TGRS.2015.2472532.